FACULTY OF SCIENCE
UNIVERSITY OF COPENHAGEN

Master's thesis

Investigating the FeII/MgII-ratio as a possible metallicity tracer in high redshift Quasars

Anna-Sofie Köhn Zahl
Email: Zahl@dark-cosmology.dk

Submitted: April 12, 2015

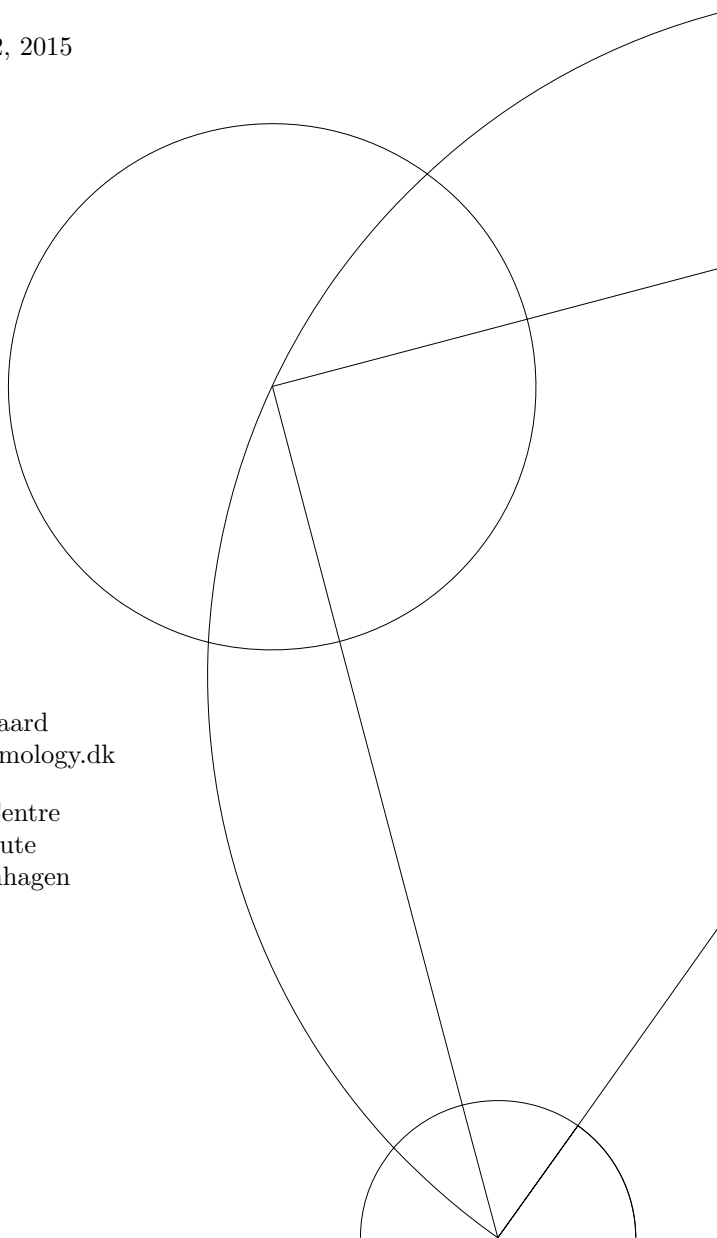

Supervisor
Marianne Vestergaard
Email: vester@dark-cosmology.dk

Dark Cosmology Centre
Niels Bohr Institute
University of Copenhagen

Abstract

The $\frac{FeII}{MgII}$-ratio have been suggested as a cosmic clock thereby it have implicitly been assumed that the ratio of UV FeII, which is measured in the range from 2000-30000 Å, and MgII 2800 Å to be a tracer of the metallicity in quasars. The focus of this thesis is to determine whether the $\frac{FeII}{MgII}$-ratio scale with the metallicity in quasars. The motivation for this investigation is that the $\frac{FeII}{MgII}$-ratio has been used as a tracer for the metallicity without compelling evidence of the existence of the relation. Therefore I examine 100 high redshift ($3.5 \leq z \leq 4.5$) quasar spectra from the XQ-100 Legacy Survey. For 95 of these quasars I could determine the metallicity based on line ratios of the broad emission lines and for 86 objects the $\frac{FeII}{MgII}$-ratio was available. In order to determine the metallicity I have used the scaling relation between specific broad emission line ratios and the metallicity (Hamann et al. 2002).

I show that the $\frac{FeII}{MgII}$-ratio is not correlated with the metallicity. This result apply to all QSOs and is statistical significant. The most likely reason why no scaling relation is present is because the FeII pseudo-continuum emission is more affected by other parameters of the gas than the abundance of Fe e.g. the microturbulence.

I also show that there is a relation between the mass and the luminosity and metallicity respectively. I further investigate if the activity, which is quantized as $\frac{L_{bol}}{L_{edd}}$, of the Quasars have a relation with the mass and the metallicity which I find that they have. This suggest co-evolution between QSOs and their host galaxies.

Contents

1. Motivation

The main objective of this thesis is to investigate the $\frac{FeII}{MgII}$-ratio and the metallicity, Z, in quasars (QSOs) in order to establish if there is a relationship for reasons outlined below. This is done using newly released X-shooter spectra from the XQ-100 Legacy survey which provide high quality spectra of 100 QSOs.

QSOs are the most luminous type of active galactic nuclei (AGNs) and are typically found at redshifts of 2-3 (Peterson 1997; Sparke & Gallagher 2007). A QSO is a galaxy with an accreting super massive black hole (SMBH) residing in its centre, see figure 1. In the figure it can be seen that a disk lies around the SMBH, which is known as the accretion disk. Mass is accreted by the SMBH from the disk. As the gas falls into the SMBH the gravitational energy of the material is partly released as radiation. The radiation from the accretion disk can then interact with the surrounding gas in the broad line region (BLR) and narrow line region (NLR) (see figure 1). The interaction with the BLR creates characteristic broad emission lines (BELs) which can be used to obtain both metallicity estimates of the BLR and mass estimates of the SMBH.

The reason why it is interesting to investigate the $\frac{FeII}{MgII}$-ratio is because it is believed to scale with the metallicity. The metallicity is an indicator of the star formation history (Hamann & Ferland 1999). The star formation history is believed to be related to galaxy evolution. Therefore the metallicity is an important parameter in relation to galaxy evolution and formation. At an early point in the evolution history of galaxies all galaxies are believed to have had an active nucleus. Thus actively accreting SMBHs can be seen as young galaxies where all the accreting gas has not yet fallen into the SMBH. With this line of thought it would make sense if the relations observed in galaxies was present in QSOs (Hopkins et al. 2006, 2007). One of these relations is the $\frac{FeII}{MgII}$-ratios scaling with the metallicity. This relation has previously been used to estimate the metallicity in QSOs even though the relation has not been proven to exist. A relation between the $\frac{FeII}{MgII}$-ratios and the metallicity is to be expected because AGNs are the inner part of high mass galaxies. The reason why no relation have been observed may be because of the limitations of the methods used to measure the metallicity of QSOs, or in the different methods used to measure the metallicity in QSOs and galaxies. In QSOs the metallicity is typically measured in the BLR from ratios of specific BELs whereas in galaxies it is measured from absorption lines, either originating from the bulge or the disk.

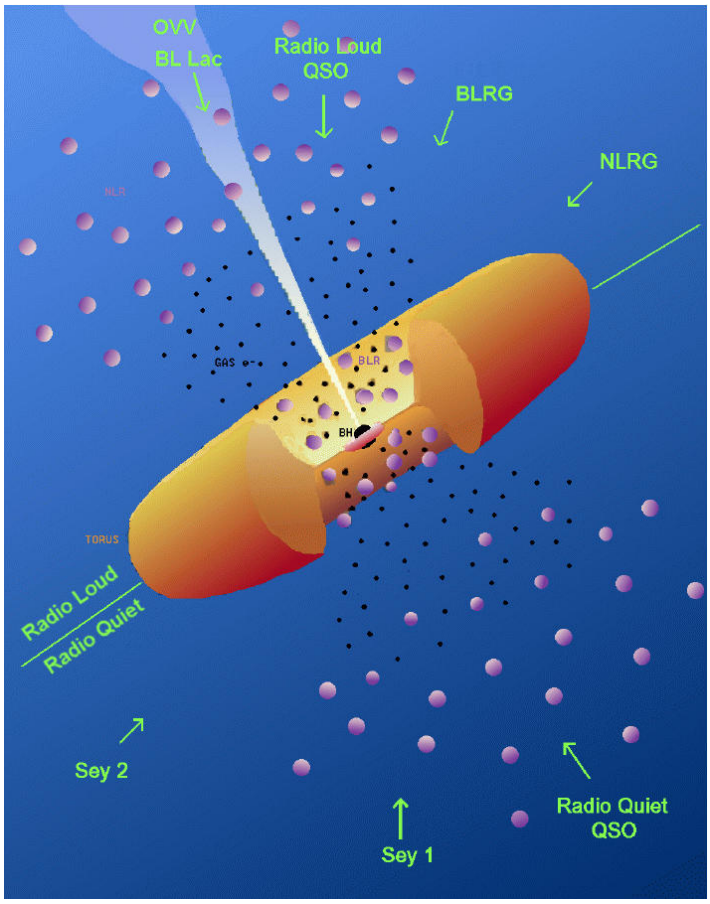

Fig. 1.— A schematic overview of the taxonomy of an AGN, with the different types dependent on the viewing angle depicted on the figure. The figure is from Urry & Padovani (1995). Note the meaning of the abbreviations are: Sey means Seyfert Galaxy, which is a type of AGN that is less luminous than QSOs, and BL Lac objects are a type of AGN where the continuum is dominant and no emission lines can be seen.

The relation between the $\frac{FeII}{MgII}$-ratio and the BLR gas metallicity has been investigated by Dietrich & Hamann (2008) for a sample of 11 QSOs, where the metallicity was obtained from the BELs: OVI, NV, NIV], CIV, HeII, OIII], NIII] and CIII][1]. Specific ratios of the line strengths have been shown to scale with the metallicity (Hamann et al. 2002). In order to obtain the $\frac{FeII}{MgII}$-ratio, Dietrich et al. (2003d) modelled the FeII pseudo-continuum and the MgII doublet was then fitted after the FeII had been subtracted (this method will be used in this work). The results of this can be seen in figure 2. From these data it cannot be determined if there is a relation, hence a statistically significant sample is needed.

[1]Here] denotes semi-forbidden emission lines.

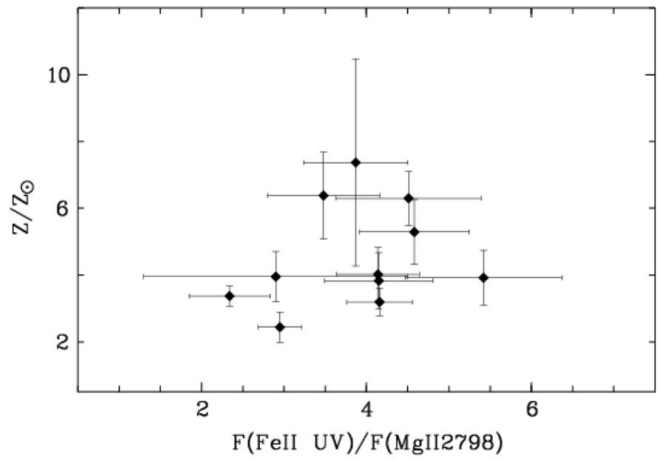

Fig. 2.— The figure is from Dietrich & Hamann (2008) and shows the metallicity as a function of $\frac{FeII}{MgII}$ for 11 sources. It can here be seen that it is unclear whether there is any relation. A larger, i.e. statistically significant, sample is needed in order to establish the reality of a correlation.

The $\frac{FeII}{MgII}$-ratio has neither been proven nor rejected to have a relation with the metallicity because it has not been possible to obtain the required data. This was made possible with the arrival of the X-shooter instrument which was created in 2009 and is a partly Danish project (Verner et al. 2011). X-shooter provides spectral coverage from 310-2400 nm (Verner et al. 2011). It is especially the broad wavelength range in which X-shooter can observe that is the key feature required for this investigation. In the papers by Dietrich et al. (2003b,a,d) the massive amount of work required to combine the spectra can be seen (Dietrich et al. 2003b,a). This extra work has been made obsolete and is a major advantage because metallicity estimates as well as the $\frac{FeII}{MgII}$-ratio needs to be obtained for a statistically significant number of sources. X-shooter has been used for the XQ-100 Legacy survey which has observed 100 QSOs. In October 2014 the telluric corrected data were provided to the collaboration. Thus these results are very new.

2. Introduction

In this section I provide the necessary background for the current study. I start with an introduction to AGN and their observed continuum and line emission because they are essential for the current study. This is followed by a section about the metallicity which introduces the basics of metallicity and why it is such an important

parameter. In this section the evolution of the interstellar medium (ISM) is explained and how the metals are produced and mixed into the ISM. This followed by two subsections explaining how the metallicity can be measured from the broad emission lines and which emission line ratios have been shown to scale with the metallicity and why this makes sense theoretically. The next subsection introduces $\frac{FeII}{MgII}$ why it has been thought to scale with the metallicity and the arguments against a scaling relation. Because I later analyse how the metallicity estimates potentially relate to the black hole mass and the mass accretion rate, parametrized as the Eddington luminosity ratio, I outline in section 2.3 how the black hole masses are determined. The last section summarises – some of – the main points and explain the objective of the study.

2.1. Quasars

When quasars were discovered they were identified as radio emitters and named quasi-stellar-objects (Peterson 1997; Davidson & Netzer 1979). Quasi means resembling, so a quasi-stellar-object means an object resembling a star and is abbreviated as QSO. QSOs are point sources and was in this regard thought to resemble stars (Davidson & Netzer 1979). But when investigating their spectra it was clear to be of non-stellar origin because of their very broad lines and characteristic continuum spectra (Peterson 1997).

QSOs are the most luminous subclass of AGNs with luminosities of $\sim 10^{47}$ ergs$\cdot$ s^{-1} or more (Peterson 1997; Shlosman et al. 1990). They emit continuously in a very broad range of the spectrum from radio to γ-rays (Longair 2000). The majority of QSOs have redshifts around 2-3 but have been observed with a redshift as high[2] as 7.085 (Peterson 1997; Bell 2004; Mortlock et al. 2011). In comparison the most distant object observed is the Gamma Ray Burst, GRB090423, with a redshift of 8.2 (Tanvir et al. 2009).

QSOs are situated in the centre of galaxies (Peterson 1997). But since QSOs typically are observed at high redshifts their host galaxies can rarely be observed. This is because the strong emission from the QSO outshines the host galaxy and because the surface brightness dimming with redshift (Sparke & Gallagher 2007). QSOs are believed to be the adolescence of galactic nuclei. But it is unknown if this is a stage all large galaxies have undergone or if it is just some galaxies (Longair 2000). QSO studies and galaxy formation history are intertwined fields. This is a motivation for

[2]This is the redshift of the most distant observed QSO ULASJ112001.48+064124.3 (Mortlock et al. 2011)

investigating whether QSOs and galaxies share some of the same relationships. They have been shown to have the mass-luminosity relation in common (Hamann & Ferland 1999). But this relation is in some sense quite universal i.e. bigger is bigger. So whether they share the relation because they are the same type of objects at different evolutionary stages or if there is another reason behind is unknown.

All AGNs and QSOs have the same basic structure (see figure 1). In the centre resides an SMBH with a surrounding accretion disk. The accretion disk feeds the SMBH with gas, which is heated up as the gas falls into the SMBH (Peterson 1997). Further out lies the BLR and thereafter the NLR. The BLR can be described as a collection of gas clouds distributed around the centre well within ~ 1 pc. There is some discussion on whether the BLR actually consists of a lot of small clouds or if it is rather a disk wind (Hamann & Ferland 1999). But the emission lines can be created in much the same way in both systems. We know the BLR gas contains metals, has high densities and a high velocity dispersion (Hamann & Ferland 1999). The high velocity dispersion creates the broad lines via Doppler line broadening, hence the name broad emission lines (Peterson 1997). The NLR lies further out at hundreds of parsecs and is thought to consist of larger clouds with a smaller velocity dispersion (Peterson 1997). The lower velocity dispersion of the gas gives rise to the narrow emission lines of the NLR. The emission line origin will be explained further in section 2.1.2. Surrounding the BLR is the torus which is a torus shaped gigantic gas structure (again see figure 1). Lastly there can be radio jets which are extended linear structures (Peterson 1997). The inner part of a jet is associated with high, mostly relativistic, velocities and the outer parts form radio lobes of isotropically emitting electrons deposited by the radio jet. The radio lobes are created when the ejected relativistic particles loses enough energy to become non-relativistic. This can happen when the ejected relativistic particles collide with the ISM or intergalactic medium (Peterson 1997). It is important to understand the taxonomy of QSOs since it is the combined contribution of the emission and absorption of the different regions and structures that creates the spectrum of QSOs where the individual regions are typically not possible to spatially resolve.

QSOs can be divided into two overall groups, one with broad lines and one without, which is referred to as Type 1 and Type 2 AGNs respectively. The reason why some QSOs show broad emission lines in their spectre and others do not is primarily due to the viewing angle. Here, for Type 2 objects, the torus obscures our view of the broad line emitting gas. Therefore the objects of interest for this thesis are the ones which have BELs in their spectre. The BELs enable measurements of the $\frac{FeII}{MgII}$-ratio and the metallicity of the BLR which is most closely attached to the QSO in comparison to the NLR (which could also be affected by the host galaxy because the NLR spans very

large spatial scales).

2.1.1. AGN Continuum

The continuum emission is created by the accretion disc (Emerson 1996). The energy driving the QSO is the accretion of mass onto the SMBH (Peterson 1997). As a particle falls towards the SMBH it looses potential energy. If there was no other particles or obstacles the particle would simply gain kinetic energy and be absorbed by the central SMBH. But for a particle in the disk there are many particles blocking its path towards the SMBH. Therefore the particle experiences collisions with other particles i.e. friction which heats up the gas. The heat is radiated away as a black body with luminosity, L, of (Peterson 1997):

$$L = \frac{GM\dot{M}}{2r} = 2\pi r^2 \sigma T^4 \tag{1}$$

where G is the gravitational constant, M is the mass of the accretion disk, $\dot{M}$ is the mass accretion rate, r is the distance of a particle or cloud of gas from the central SMBH, T is the temperature. Furthermore σT^4 is the energy radiated away per unit area, πr^2 is the area of the disc and the preceding factor of two accounts for the fact that the disk has two sides (Peterson 1997). It is assumed that the released energy of a particle at distance r from the central source is dissipated locally and that the medium is optically thick (Peterson 1997).

If we then assume thermodynamic equilibrium in an annulus of the disc we can approximate the local emission as black-body radiation. This means that the spectrum of this annulus only depends on the temperature and wavelength (Peterson 1997):

$$I(\nu, T) = \frac{2h\nu^3}{c^2} \cdot \frac{1}{e^{\frac{h\nu}{kT}} - 1} \tag{2}$$

The shape of a black body spectrum can be seen in figure 3. The accretion disk is made up of several different blackbodies since the disk has multiple annuli all with different temperatures, where the hottest annulus is the innermost and the coolest is the outermost. The combined contribution of different blackbodies with randomly chosen temperatures is also presented in figure 3 as an example.

The intensity of the continuum emission is higher in the blue region and falls of in the shape of a power law towards the red part of the spectrum (Peterson 1997). The slope of the power law has been investigated by De Rosa et al. (2011) who have

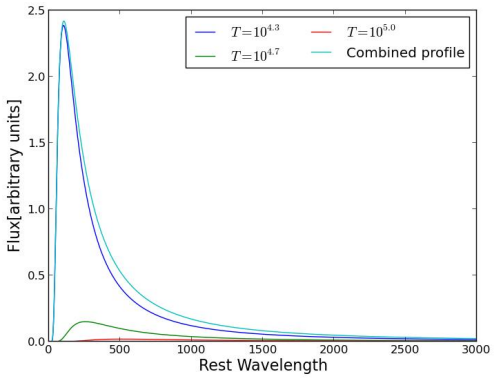

Fig. 3.— The black body with three different temperatures and the combined profile.

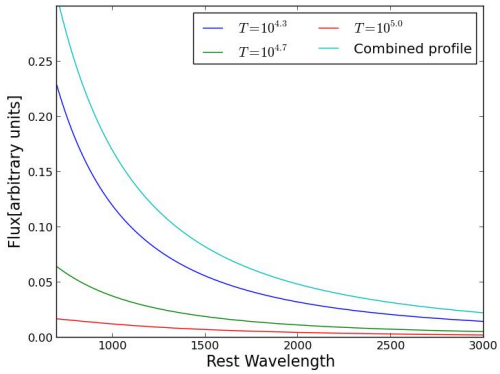

Fig. 4.— The zoom in on the figure to the left.

found an average slope of -1.3, which is in units of wavelength and will be throughout the thesis. This can, however, be affected by reddening by dust since dust absorbs and reflects more of the blue light than the red, leading to a "red" continuum. A red continuum is simply a continuum with more red than blue light. Some continua are very shallow but if this is an effect of the accretion or if it is caused by reddening by dust is hard to tell from a short ranged spectrum. Investigations of the continuum shape can be complicated by emission and absorption lines in the spectrum. This is especially true if they are broad lines since their wings can contaminate parts of the spectra used for modelling of the continuum emission. This will be further explained in section 3.2.2.

2.1.2. AGN Emission Line Origin

The most important feature of the spectrum for this study is the emission lines. The BELs can be used to estimate the metallicity and the mass, therefore obtaining an extensive knowledge about them is essential for this study.

The BLR consists of metal enriched gas situated close to the central SMBH. It has a high degree of velocity dispersion which creates the characteristically broad lines seen in QSO spectra, see figure 5. The observed line widths are caused by bulk motions of the gas which have typical velocities in the range of 1000 to 5000 km·s^{-1} but can reach widths up to 10000 km·s^{-1} (Emerson 1996). Typical densities of clouds in the BLR is in the range of 10^8 to 10^{12} cm^{-3} (Hamann & Ferland 1999).

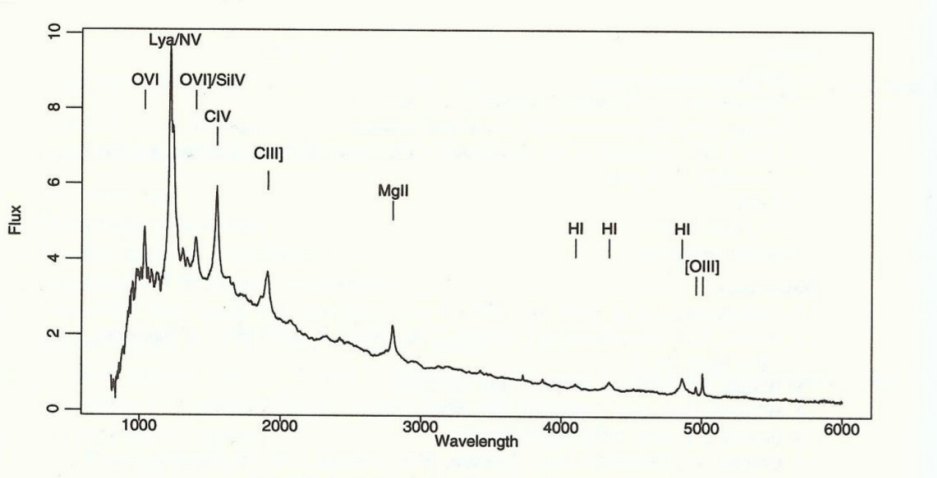

Fig. 5.— A typical spectrum of an AGN with the power law shaped continuum and the emission lines consisting of both a narrow and a broad component. This figure is from (Cox 2000).

The energy source responsible for the BLR emission is photoionization by the continuum radiation from the central source (Peterson 1997). Photoionization is the physical process in which an ion is formed from the interaction of a photon with an atom or molecule (Emerson 1996). In a QSO the photons originating from the disk reach the BLR which ionize the gas. The gas then radiates photons with specific energies according to the transitions of the atoms present in the gas. The strength and shape of the line is determined by the composition, physics and velocity profile of the gas. The main evidence for this is that the emission line spectra seem to be dependent on the continuum variability. Because the emission line strengths and shapes changes in response to changes in the continuum intensity with lag times corresponding to characteristic radii of the BLR (Peterson et al. 1993).

The emission line profile of an element depends on the density of the gas, the chemical abundance, the velocity field and in some cases it is also sensitive to the gas temperature. Korista et al. (1997) have made an atlas of computed equivalent widths of QSO BELs based on several thousand photoionization calculations. There it can be seen where in the density-radiation plane the transition will be the most dominant (Korista et al. 1997). If we compare specific transitions it is also possible to see which transitions are likely to be created in the gas under the same conditions i.e. same distance from the centre, photon-flux and density leading to similar velocity profiles. If two emission lines should have the same profile according to Korista et al. (1997) it justifies using a template to fit another line with the same velocity profile. This can be important because some of the emission lines form complexes with other lines e.g.

NV blends heavily in the red wing of Ly-α. Therefore modelling the NV and Ly-α lines with a template that is known to have the same velocity profile is more exact than randomly modelling each transition with a profile, e.g. a Gaussian function. This is relevant to the data processing and data analysis for this study and will be further elaborated in section 3.

2.2. Metallicity

The metallicity of the ISM is a measure of the amount of metals in the gas (Stahler & Palla 2005). The metals are primarily a product of stellar processes since very little was created during the Big Bang. Enrichment of the ISM may happen when a Super Nova (SN) explodes. In a SN explosion, metals are thrown out from its centre to be incorporated into the ISM. The wind created from the SN can be shocked when it reaches e.g. a molecular cloud, which can also be shocked, and in some cases star formation can be triggered (Sparke & Gallagher 2007). As time passes more stars are created and some of these enrich the neighbouring gas when the SN explode. This ongoing chemical enrichment of the ISM is sometimes referred to as the enrichment cycle (Hamann & Ferland 1999). For a steady rate of SN the chemical enrichment would scale with time. The SN rate is, however, not believed to have been constant at all times hence the metallicity is not a direct measure of time. The metallicity can say something about the evolution history of a gas. If the metallicity is very high it shows that the gas has been through numerous generations of stars. A high metallicity could either have been created due to a high SN-rate in a relatively short time or have build up due to continuous starformation for a very long time. If the observed entity is of very high redshift it must be the first scenario since there would not have been time for a steady evolution of the metallicity. Hence the metallicity can be used as a measure of the star formation history (Hamann & Ferland 1999).

Quasar emission line spectra are quite similar over a wide range of redshifts and luminosities (Hamann & Ferland 1999; Dietrich et al. 2003b). This could either suggest that the sources have a very similar composition of metals or that the emission lines used to determine the metallicity are insensitive to the actual abundance (Verner et al. 2003; Baldwin et al. 2004). The metallicities measured is typically solar or supersolar hence some enrichment must have taken place.

Measuring the metallicity of the ISM directly by its emission is not possible. The reason being that the ISM radiates very little since it is typically very cool with a mean temperature around 100K (Sparke & Gallagher 2007). A method of obtaining

the metallicity of the ISM is by using a background source. This could e.g. be a QSO which would enable us to investigate the ISM at very high redshift. Intervening matter can be observed in QSOs in narrow absorption lines in the spectrum or as Damped Lyman-α absorbers (DLAs) which is thought to be galaxy halos or very young galaxies (Longair 2000). The metallicity can be derived from the absorption lines from the DLA (Longair 2000). This is different from the method used when determining the metallicity of QSOs where the BELs are used. This is because the absorption lines in QSOs are not well understood, not as common as BELs and their formation regions are not well-defined (Hamann & Ferland 1999). Therefore there is a clear advantage by using BELs for metallicity estimates even though it is much more difficult than for DLAs or other objects using absorption lines to estimate the metallicity. This is because the absorption lines used in that case are narrow in comparison to BELs of QSOs. Narrow lines are intrinsically easier to fit or model than broad lines. Broad lines can have unruly wings to deal with as well as uneven velocity profiles, since they are broad the likelihood that they blend or makes complexes with other broad lines is higher. The origin of the broad absorption lines are associated with much more unknowns than the BELs. The region where the absorption originates from is not well defined leading to many crucial unknown factors such as the density, velocity and partial coverage. All these unknowns makes it difficult to isolate each of the contributions from the broad absorption lines. By measuring the BLR we know the measurements are from the AGN itself rather than from its host galaxy, which may be the origin of some of the broad absorption lines this is the reason why the BELs are used for metallicity estimations.

2.2.1. Metallicity Estimates Based on BEL

The abundance of an element is defined as the relative amount of that metal compared to hydrogen, N(Metal)/N(H) (Emerson 1996). The mean metallicity of stars is typically described by the abundance of iron in comparison to hydrogen i.e. N(Fe)/N(H). This is because iron is easy to detect and the abundance of heavier elements are relatively similar from star to star (Sparke & Gallagher 2007). For galactic regions the O/H-ratio is used as the mean metallicity since it is a better measure of the overall abundance of metals than Fe/H is. This is because there is a significant delay in the enrichment of Fe since it is primarily produced in SN Type Ia (Hamann & Ferland 1999), which has a timedelay of around 2-4 Gyr since a white dwarf is needed in order for this type of SN to be created (Scannapieco & Bildsten 2005).

Table 1: The created and used scaling relations for the line ratios with the metallicity

Scaling relations created by Hamann et al. (2002)	$\frac{NII]}{CII]}$,	$\frac{NIII]}{CIII]}$,	$\frac{NIII]}{OIII]}$,	$\frac{NIV]}{OIII]}$,	$\frac{NIV]}{OIV]}$,	$\frac{NIV]}{CIV}$,
	$\frac{NIII}{CIII}$,	$\frac{NIII}{OIII}$,	$\frac{NV}{HeII}$,	$\frac{NV}{CIV}$,	$\frac{NV}{OVI}$,	$\frac{NV}{(CIV+OVI)}$
Emission line ratios used in this thesis	$\frac{NIII]}{CIII]}$,	$\frac{NIII]}{OIII]}$,	$\frac{NIV]}{OIII]}$,	$\frac{NIV]}{CIV}$,	$\frac{NV}{HeII}$,	$\frac{NV}{CIV}$

In QSOs the N/O-ratio is used as a measure of the mean metallicity of the BLR (Shields 1976), since the N/O abundance is known to scale with O/H in galactic HII regions (Hamann et al. 2002). This can be explained on the assumption that nitrogen is a product of secondary nucleosynthesis in high mass stars (Shields 1976). The fusion process in high mass stars is via the CNO cycle[3]. In this process C, N and O acts as a catalyst for hydrogen burning (Stahler & Palla 2005). When the star exhausts the hydrogen it enters a range of unstable phases where most of the original oxygen and carbon is fused into nitrogen (Shields 1976). Therefore the abundance of nitrogen ejected into the ISM should scale with the abundance of oxygen in the primordial gas (Shields 1976).

Since carbon and oxygen follow the same evolution it has been investigated whether N/C $\propto$ O/H holds (Shields 1976), which is motivated by the fact that additional line ratios improve statistics making the final results more robust. Unfortunately the N/C ratio is not as robust as N/O but can still be used as a metallicity indicator (Hamann et al. 2002; Hamann & Ferland 1993b). The complication is that C/O increases as the system evolves, since the ISM is enriched with carbon in another stellar process than SN (Hamann et al. 2002; Hamann & Ferland 1993b). Carbon can be formed in the envelopes of longer lived intermediate mass stars (Stahler & Palla 2005). These stars can enrich the ISM when they enter their last phase of life (Stahler & Palla 2005). Here the stellar atmospheres expand and subtract leaving some of the outer atmosphere behind which is mixed into the ISM thereby enriching it (Stahler & Palla 2005).

Lastly $\frac{NV}{HeII}$ can be used for metallicity estimations. Here it is curious to note that N/He scales with Z^2 and $\frac{NV}{HeII}$ scales with Z (Hamann et al. 2002). It is important to mention that Hamann & Ferland (1999) and Hamann et al. (2002) via photoionization

[3]This process is only possible for high mass stars containing C, N and O.

calculations have shown that the mentioned scaling ratios are good measures of the metallicity. This is tied to the energy balance of the BLR (Hamann et al. 2002). So to summarize the line ratios that can be used as mean metallicity estimates are N/O, N/C and N/He. As these line ratios only scale with the metallicity it is crucial to have the scaling relation for specific line transitions with the metallicity. Hamann et al. (2002) have created the scaling relation between the emission line ratios and the metallicity for QSOs, which is presented in table 1. The reason why these line ratios are used is because they are present in our spectra from the XQ-100 Legacy Survey. The scaling relations for the used line ratios are presented in figure 6.

The scaling relations have been created on the basis of three different continuum models: the hard power law, the segmented power law and an empirical power law created by Mathews & Ferland (Mathews & Ferland 1987). The hard power law has a steep slope with a power of -1 (Hamann et al. 2002). The segmented power law has three different segmentations with different power indices, α, see table 2 (Hamann et al. 2002). The power law by Mathews & Ferland is the continuum proposed by Mathews & Ferland (1987) this has a blue bump from 200-1000 Å and is based on the continuum of "classical" QSO spectra as described in their work. Hamann et al. (2002) assume the broad emission line region (BELR) is free of dust and photoionized by the QSOs' continuum radiation. It is also assumed that the Doppler broadening is strictly thermal (Hamann et al. 2002).

The main challenge for BEL abundance work is that the metal lines cannot become uniformly stronger as the metallicity increases above a few percent of solar (Hamann & Simon 2010). This is because the metal lines control the cooling and would violate the balance between the energy absorbed and emitted by photoionized BEL clouds (Hamann & Simon 2010).

Table 2: Power indices for the segmented power law

λ_{ranges} [Å]	0.2479-12.398	12.398-912	912–10000 Å
α	0.9	1.6	0.6

2.2.2. $\frac{FeII}{MgII}$ *a Metallicity Indicator*

In models of galactic chemical evolution the Fe to alpha-element ratio can be seen as an indicator of the metallicity of star forming systems (Wheeler et al. 1989; Verner et al. 2003). Here an alpha-element means an element such as O, Mg and Si (Hamann & Ferland 1993b). The Fe to alpha-element ratio has also been shown to scale with

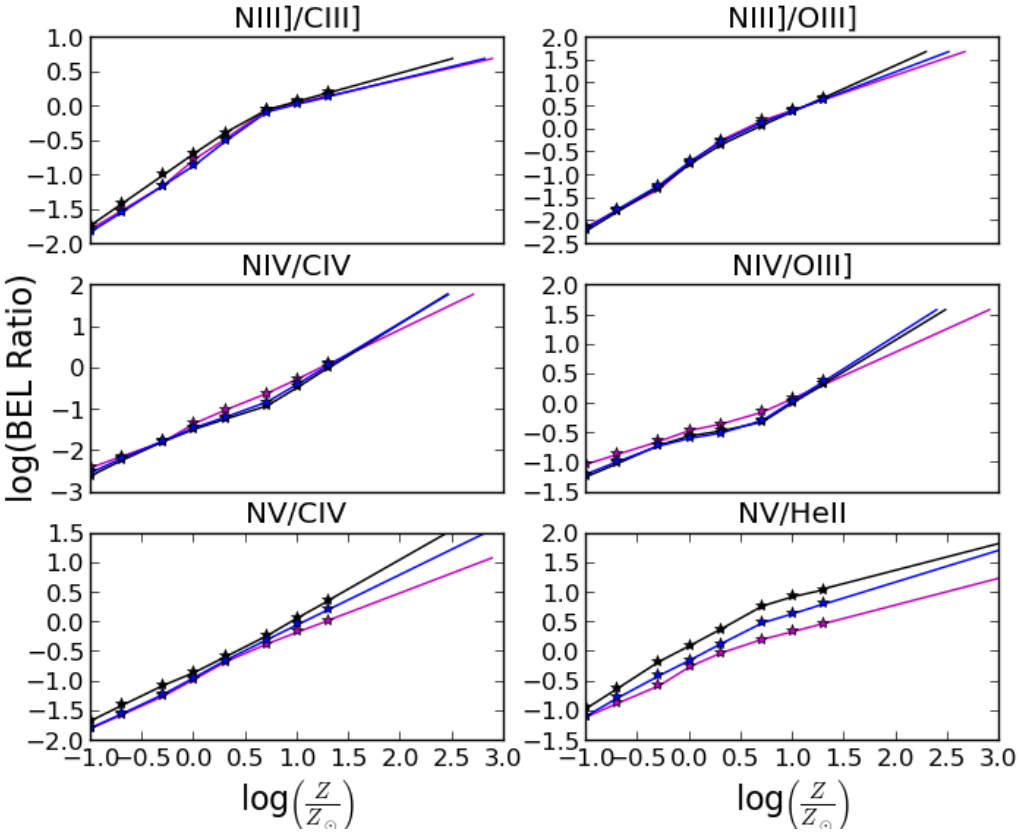

Fig. 6.— The scaling relation between the emission line ratio and the metallicity for the line ratios used in this thesis. The three lines is for three different continuum models: the hard power law (black line), the power law created by Mathews & Ferland (magenta line) and the broken power law (blue line). The data is from Hamann et al. (2002).

the metallicity in galaxies (Sparke & Gallagher 2007). Galaxies and QSOs are believed to have a high degree of co-evolution and both have a mass-luminosity relation and may exhibit other relationships e.g. the mass-metallicity relation (Hamann & Ferland 1999). This makes it obvious to investigate if QSOs share the Fe to alpha-element ratio to metallicity relation. But there are some differences in how we observe the Fe to alpha-element ratio that may affect if a scaling with the metallicity is present. In galaxies the abundances are measured in relatively narrow absorption lines of the ISM and in QSOs it is measured from the BELs from the nuclear region around the BH (as described in section 2.2.1).

Besides co-evolution of QSOs with galaxies it makes sense that the Fe to alpha-element ratio should scale with the metallicity, since the formation channels of Fe and

the alpha-elements are different. Fe is primarily a product of SN type Ia whereas the alpha-elements are produced in SN type II. The delay of SN type Ia, in comparison to SN type II, as previously mentioned is around 2-4 Gyr (Scannapieco & Bildsten 2005). This should lead to an increase of the Fe to alpha-element ratio at the onset of Fe production. If the production of Fe and the alpha-elements is continuous the Fe to alpha-element ratio should scale with the metallicity. In order to measure the Fe to alpha-element ratio the typical lines measured have been FeII and MgII since these are believed to be the most reliable tracers of the Fe and Mg abundances respectively (Hamann & Ferland 1993b). FeII forms a pseudo-continuum ranging from 2000 Å to 3000 Å which has been described by Verner et al. (2003) and Vestergaard & Wilkes (2001). The reason why a pseudo-continuum is formed from FeII is because Fe is a complex atom with 26 electrons this leads to many thousands of possible transitions which lie very close together in energy. All the small FeII lines blend due to the high velocities of the BLR gas thereby forming a higher flux level in a range; therefore it is referred to as a pseudo-continuum. Vestergaard & Wilkes (2001) have created a model of the FeII pseudo-continuum from the emission spectrum of the narrow line Seyfert galaxy I Zwicky 1. This model can be used to determine the line strength of the FeII pseudo-continuum for QSO spectra. MgII is a broad emission line which lies at 2797.92 Å. It's location in the middle of the FeII pseudo-continuum makes it difficult to measure the line profile of MgII.

The $\frac{FeII}{MgII}$-ratio has previously been used as a metallicity tracer (Hamann & Ferland 1993a). But it has not been determined whether the relation holds and therefore caution should be taken about using the relation without reservation (De Rosa et al. 2011, 2014; Dietrich et al. 2003a). Verner et al. (2003) have raised concern about the $\frac{FeII}{MgII}$-ratio being a tracer for the metallicity, since the FeII strength is dependent on not only the abundance but also the microturbulence and radiation effects (Verner et al. 2003). Baldwin et al. (2004) state:

"Photoionized BELR clouds cannot produce both the observed shape and observed equivalent width of the 2200–2800 Å Fe II UV bump unless there is considerable velocity structure corresponding to a microturbulent velocity parameter $v_{turb} \geq 100 km\ s^{-1}$*."*

Hence if FeII is highly dependent on microturbulence and it is present, the $\frac{FeII}{MgII}$-ratios possible scaling relation with the metallicity seems a lot less likely. The microturbulence may not be as strong as Baldwin et al. (2004) state because Ferland et al. (2009) have shown that the FeII(UV) bump can be explained if inflows/outflows are included in photoionization model calculations. But this still makes the FeII emission dependent on other effects than the FeII abundance.

2.3. Mass Estimation of Super Massive Black Holes in AGNs

As a part of my analysis I investigate how the metallicity scales with the SMBH mass, the luminosity and the slope of the continuum. The mass-luminosity relation has been shown to exist for QSOs (Hamann & Ferland 1993a). Hence checking if the relation is present in our sample is a great way to make sure the XQ-100 Legacy survey sample is representative for QSOs.

The mass of a gravitationally bound object can be determined using the virial theorem or Kepler's laws. The variables needed to perform a mass determination of an object are the radius of the orbit, the eccentricity and the velocity of a test particle. The test particle in question could e.g. be a star that was gravitationally bound by a central SMBH. For this kind of determination a very high spatial resolution and a lot of observations over time would be required. This method of obtaining the SMBH mass is called a direct method and has been used alongside other methods to obtain the mass of the central black hole of our galaxy (Peterson 2011). The different types of mass determinations are named after how direct the method is and how many assumptions are necessary to obtain the mass (Peterson 2011). The method that uses stars to determine the SMBH mass, can only be used for low redshift objects because high spatial resolution is necessary, since this method is dependent on tracking the orbit of the star.

For QSOs this method is not possible to use since they are of too high redshift and measurements of stars in close orbit around them are impossible (even if the BLR consisted of stars the problem of spatial resolution remains). So for mass estimation of objects with high redshift another gravitationally bound test particle than a star is needed. The most promising test particle of the SMBH must be the BLR gas. These can however be affected by radiation pressure and winds from the accretion disk. Netzer & Marziani (2010) have investigated the effect of the photon pressure on the BLR and find that it is minimal, validating the assumption that the BLR is primarily affected by gravity.

If we assume that the BLR clouds have circular orbits the problem is simplified a bit. Hence the velocity dispersion and the radius of the BLR are the only parameters needed. The velocity dispersion can be determined from the FWHM or the line dispersion, σ_l, of the BELs, because the emission lines are broadened by Doppler line broadening. Doppler line broadening is caused by velocities of the atoms of the

line emitting gas[4]. The radius can be determined from the radius-luminosity relation (Bentz et al. 2013). So for a gas cloud gravitationally bound by a SMBH the formula is (Vestergaard & Osmer 2009):

$$M_{BH} = \frac{f R_{BLR} \Delta V^2}{G}. \tag{3}$$

Here M_{BH} is the mass of the central SMBH, f is a scale factor of order unity, R_{BLR} is the radius of the BLR, ΔV is the emission line width and G is the gravitational constant. For ΔV either the FWHM or the line dispersion, σ_{line}, can be used, where σ_{line} is believed to provide the most accurate result (Peterson 2011). The radius-luminosity relation[5] $R \propto L_\lambda^\alpha$ (Kaspi et al. 2005) where $\alpha \sim 0.5$ can be used to provide R_{BLR} (Peterson 2011). Hence the radius is replaced with L_λ^α in equation 3. Therefore we need the flux-luminosity relation because the flux is the observed quantity:

$$L_\lambda = 4\pi F_\lambda d_L^2 (z+1). \tag{4}$$

Here, the luminosity distance, d_L, is a cosmological parameter which can be expressed using Hubble's law for the nearby universe or the luminosity distance relation to the transverse co-moving distance for the distant universe (Hogg 1999). The equation describing the luminosity distance for the distant universe:

$$d_L \approx (1+z) D_M, \tag{5}$$

where z is the redshift and D_M has an analytical solution for a flat universe and $\Omega_\Lambda = 0$, which is the density parameter of the cosmological constant Λ:

$$D_M = D_H \frac{2[2 - \Omega_M(1-z) - (2-\Omega_M)\sqrt{1+\Omega_M z}]}{\Omega_M^2 (1+z)} \qquad \text{for } \Omega_k = 0 \text{ and } \Omega_\Lambda = 0, \tag{6}$$

where Ω_M is the matter density, Ω_k is the curvature of the universe, here $\Omega_k = 0$ means a flat universe, and D_H is the Hubble distance:

$$D_H = \frac{c}{H_0} = 3000\ h^{-1} Mpc, \tag{7}$$

where H_0 is the Hubble parameter. We now have the equations necessary to calculate the SMBH mass. Hence the next step is to determine which emission lines to use.

[4]When atoms moves away from the observer it leads to redshifted emission lines and if they move in the direction of the observer it leads to blue shifting of the emission lines. If the direction of the movements are random the combined contribution of the different velocities of the atoms leads to symmetric line broadening.

[5]Here the luminosity is the monocromatic continuum luminosity typically measured at 1350 Å, 2100 Å or 5100 Å.

In order to determine the SMBH mass, M_{BH}, BELs are needed. Not all BELs can be used since a mass scaling relation only has been created for Hβ, MgII and CIV (Vestergaard et al. 2011). Hβ is at 4861.32 Å, hence it is too far out in the red to be present in most of our sources (Cox 2000). With the MgII and CIV broad emission lines in our spectra, we can obtain the masses and get an average mass determination on the basis of both lines. Using both lines provide a more robust mass estimation since no broad line is perfect (Vestergaard & Osmer 2009; Vestergaard et al. 2011).

We have different challenges using CIV and MgII. The main challenges for using CIV for mass estimates is that it can be very blueshifted. This may be caused by winds travelling outwards in the BLR (Vestergaard et al. 2011). Hence the assumption of a BLR only governed by gravitational forces no longer holds, but this may not have been a good assumption to begin with since the BLR is affected by e.g. radiation. This would lead to an underestimation of the mass of the SMBH if the measured width of the emission line is underestimated (Vestergaard et al. 2011). The challenges for an accurate measurement of the velocity of the MgII gas is that the line profile is heavily blended with the FeII pseudo-continuum. According to Vestergaard & Wilkes (2001) the level of the FeII pseudo-continuum under the MgII emission line is at most 15-20% of the peak hight of the FeII pseudo-continuum on either side of MgII. If MgII is fitted using FeII as a point of reference roughly 50% of the MgII emission line flux is ignored (Vestergaard & Wilkes 2001). Therefore it is crucial to model the FeII and MgII emission lines. Otherwise it is impossible to obtain accurate measures of the emission line strengths. The issues with measuring the mass on the basis of the individual lines should diminish when taking the average of the mass estimate from the two lines.

So even though the two lines have some issues we can still use both of them for our investigation, since these issues does not make the methods invalid. Because Vestergaard & Peterson (2006) have shown that the SMBH mass estimates obtained from equations 8 and 9 reproduce the mass estimates from reverberation-based mass estimates[6] to within a factor of 3. Hence the calibrated mass scaling relationship for CIV and MgII is needed which for CIV is provided by Vestergaard & Peterson (2006):

$$\log(M_{BH}(CIV)) = \log\left(\left[\frac{FWHM(CIV)}{1000\ \mathrm{km\cdot s^{-1}}}\right]^2\left[\frac{\lambda L_\lambda(1350\text{Å})}{10^{44}\ \mathrm{erg\cdot s^{-1}}}\right]^{0.53}\right) + (6.66 \pm 0.01) \quad (8)$$

where $\lambda L(\lambda)$ is the continuum flux near the line, namely at 1350 Å for CIV. The constants added to each of the mass estimations are scaling factors to the zero point.

[6]Reverberation-based mass estimates uses the variability in brightness to determine the SMBH mass of nearby QSOs (see e.g. (Gebhardt et al. 2000)).

The scaling relation for MgII is presented in the work of Vestergaard & Peterson (2006) as:

$$\log(M_{BH}(MgII)) = \log\left(\left[\frac{FWHM(MgII)}{1000\ \mathrm{km}\cdot\mathrm{s}^{-1}}\right]^2\left[\frac{\lambda L_\lambda}{10^{44}\ \mathrm{erg}\cdot\mathrm{s}^{-1}}\right]^{0.5}\right) + zp(\lambda) \qquad (9)$$

where $zp(\lambda)$ is the zero point scale correction dependent on the wavelength i.e. 6.72, 6.79 and 6.86 for λ being 1350Å, 2100Å and 3000Å respectively (Vestergaard & Osmer 2009). $\lambda L(\lambda)$ is the continuum flux taken for the same wavelengths. The error for the scaling factor is $\pm$ 0.55 which is higher than for the CIV scaling relation because the error of reverberation mapping has been taken into account. The error of reverberation mapping that needs to be added is 2.9 (Vestergaard & Peterson 2006). Hence 2.9 is added to the error of the zero point scale correction under the square root of the sum of the factors squared like so:

$$CIV: \qquad \log(\sqrt{2.9^2 + 0.01^2}) = 0.462$$

which is the uncertainty of the zero point scale correction for CIV. So the second term on the right hand side of equation 8 becomes: (6.66 ± 0.462).

So now we have the formulas required to do the mass estimates including the errors associated with reverberation mapping. In order to obtain the mass estimates all that is needed is the luminosity at 1350 Å for CIV and the luminosity at either 2100 Å or 3000 Å for MgII, and lastly the FWHM for both lines.

2.4. Project Description

The main purpose of the project is to measure the $\frac{FeII}{MgII}$-ratio and the metallicity and compare them to check if there is a distinct relationship between them i.e. whether a higher $\frac{FeII}{MgII}$-ratio is associated with higher metallicity of the BLR gas. This will be done for as many of the 100 XQ-100 Legacy survey QSOs as possible. The main challenges is fitting the broad emission lines and modelling the FeII pseudo-continuum. M. Vestergaard will fit the FeII pseudo-continuum using a FeII template (Vestergaard & Wilkes 2001). Hence the main focus of my data analysis is on modelling the BELs from which the metallicity is determined using the scaling relations by Hamann et al. (2002). The SMBH mass will also be determined in order to investigate whether further scaling relations exist.

3. Data Analysis

In section 3.1 the data sample and the XQ-100 Legacy survey is introduced. Then in section 3.2 the methods used to obtain the metallicity, mass and $\frac{FeII}{MgII}$ is explained in steps. The last section shows the results where it is briefly discussed whether the results are significant and how dependent the results are on the method.

3.1. Sample and Data

The data used in this thesis originates from the XQ-100 Legacy Survey. The XQ-100 Legacy Survey focused on obtaining a homogeneous sample of 100 VLT/X-shooter spectra of QSOs with redshifts in the range from 3.5 to 4.5 with spectral coverage of 310-2400 nm and a high S/N $>$ 20 (see López et. al. 2015, in preparation). The Survey was awarded 100 hours as an ESO LP within Chilean time (see López et. al. 2015, in preparation). The main scientific objectives have a wide span and include:

- Inter Galactic Medium science
  - MgII-emission line survey
  - 'Damped Lyman-α Absorbers'-survey
  - Lyman Limit System survey
- AGN science
  - Physics of Infra Red redshifted AGNs
  - Physical properties of AGN
  - Associated absorbers
- Cosmology
  - Matter power spectrum
  - Proximity effect

One of the main features of the spectra was absorption lines from intervening gas clouds i.e. DLAs which complicates the data processing and analysis since I use the emission lines. The complication was caused when absorption lines intervened with the desired emission lines because it made it more complicated to model the emission lines. Here it is important to note that there are two general types of absorption the kind which originates from e.g. an intervening gas cloud in the ISM and telluric absorption

lines which is absorption lines from our atmosphere. The telluric absorption lines posed another problem that primarily affected the part of the spectrum where FeII and MgII was measured, which is discussed in section 3.2.6.

One advantage of the data is that the spectra have high S/N ratios. In this case narrow absorption lines can, for most parts, be eliminated when modelling the emission line profiles and the continuum emission. This is described in section 3.2.2. Another crucial feature of the data was the very wide spectral coverage. This was necessary to have in order to obtain both the broad lines used for the metallicity estimates, the FeII pseudo-continuum and the MgII line. These features are very significant and crucial for our investigation. The fact that this survey provides this many high quality spectra is also very important since the number of QSO spectra used by Dietrich et al. (2003b) was the limiting factor and the reason why no correlation was determined or rejected.

3.2. Methods

The goal of the investigation is to determine the BLR metallicity, the $\frac{FeII}{MgII}$-ratio and the SMBH mass, M_{BH}. The BELs used to perform the metallicity estimation are: NV, $NIV]$, CIV, $HeII$, $OIII]$, $NIII]$ & $CIII]$. The line flux ratios was then converted into a metallicity using the scaling relations by Hamann et al. (2002)(see section 2.2.1 and figure 6). It is important to note that OVI has a line flux scaling relation but as the QSOs reside at so high redshift it was impossible to observe since OVI was completely engulfed in the Ly-α forest. The $\frac{FeII}{MgII}$ measurements were provided by M. Vestergaard 2015, private communications, see section 3.2.6. The FWHM and line dispersion was used to obtain the BH mass of the QSO using equations 9 and 8 Vestergaard & Osmer (2009).

In order to determine the line flux of the BELs it was necessary to create model fits of the emission lines. This is necessary because the lines blend with each other. Some of the emission lines are in complexes i.e. Ly-α-NV and SiII-CIII]. The weak lines around CIV can often be seen to lie in the CIV wing and lastly OIII] is often blended with HeII. Therefore simply integrating over some fixed ranges is a bad representation of the actual line flux of any of the BELs. To obtain the metallicities, the $\frac{FeII}{MgII}$-ratio and the mass for this study involves a number of subtasks that can be outlined as follows and will be described in the shown order (next page):

- Data Preparation
- Continuum Fitting
- Line Fitting
  - Creation of the CIV Template
  - Application
    - The Line Complexes of Ly-α-NV & SiII-CIII]
    - The weak lines NIV], HeII], OIII] & NIII]
- Metallicity Determination
  - Model Selection
  - Error Estimation
  - Offset calibration
  - Combination of the Metallicity Estimates
- $\frac{FeII}{MgII}$ Determination
- Mass Determination

3.2.1. Data Preparation

The very first task was to determine for which of the sources metallicity estimates and the $\frac{FeII}{MgII}$-ratio could be measured for. Sources were discarded if the redshift was too high or if there were no BELs present. I discarded objects with z>4.5 because the $\frac{FeII}{MgII}$-ratio could not be measured since MgII is shifted out of our spectral window. If there were no BELs present in our spectral window none of the desired parameters could be measured, hence it is obvious that they should be discarded. The spectra were investigated and 94 out of the original 100 sources could be used, which was very promising. Four sources: #13, #46, #48 & #77[7], were discarded due to too high redshift and just one source, #54, was discarded because it had no BELs.

The spectra received from the XQ-100 Legacy Survey came in two sub-spectra: one for the visual (VIS) part and one for the near infrared (NIR) part, where[8] VIS

[7]These are the numbers associated with the sources and the source names can be looked up in appendix A.3

[8]url:http://www.eso.org/sci/facilities/paranal/instruments/xshooter/inst.html

ranges from 550-1020 nm and NIR ranges from 1020-2480 nm. For an average source with redshift around 3.4 the VIS and NIR parts would range from 1250-2318 Å and 2318-5636 Å respectively. This would split up the FeII pseudo-continuum which ranges from 2000-3000 Å (Vestergaard & Wilkes 2001). Therefore I had to combine the VIS with the NIR in order to measure the FeII pseudo-continuum. It was also useful for the continuum fitting since continuum window E and F, in table 3, became accessible. Another advantage is that the results for the BELs are more comparable to FeII and MgII if the same continuum windows are used for the continuum fit. If different continuum windows are used for the BELs and for FeII and MgII it could result in different continuum shapes which could affect the measurements. It is therefore preferable that the continuum fit is the same for both regions.

The main challenge in combining VIS with NIR was to make sure that there were no offsets in the flux level after having combined the data. This was solved by determining the offset factor, f_{Off}, between the two sub-spectra and scaling NIR to VIS as so:

$$f_{Off} = \frac{\langle F_{VIS} \rangle}{\langle F_{NIR} \rangle} \tag{10}$$

Here F_{VIS} and F_{NIR} are the flux levels of VIS and NIR respectively for the region 10000-10200 Å. The range was chosen to be ± 100 Å around the point where the error spectrum was at its lowest for both sources, which was at 10100 Å (see figure 9) where ± 100 Å was chosen in order to have enough statistics and because this range was within the VIS and NIR ranges.

Then f_{Off} was used to correct the offset by multiplying with the NIR sub-spectrum. Thereafter the excess from both sub spectra was eliminated, which for the NIR sub spectrum was the part where $\lambda < 10100$ Å and for VIS $\lambda > 10100$ Å. The two remaining parts of the VIS and NIR were then combined and all the combined spectra were investigated in order to make sure the combination was performed correctly for all the sources. The combination frames for each of the sources can be found in appendix C and the plots showing a combination of source #4 can be seen in figures 7, 8 and 9. The source #4 was chosen because it is an example of a typical source with some offset. But the majority of the sources only had very little or no offsets so source #4 is only typical for the sources with offsets.

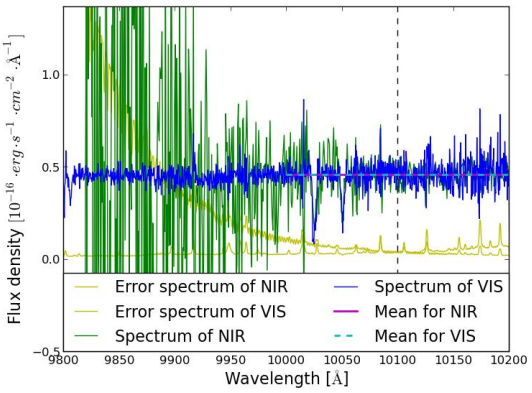

Fig. 7.— The rescaling of NIR to VIS.

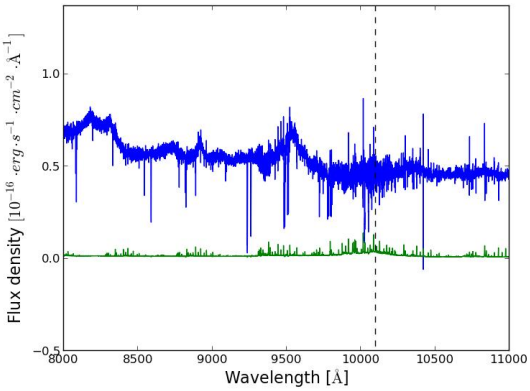

Fig. 8.— Final result of rescaling and combining NIR with VIS. The green line is the combined error spectrum and the blue is the combined spectrum.

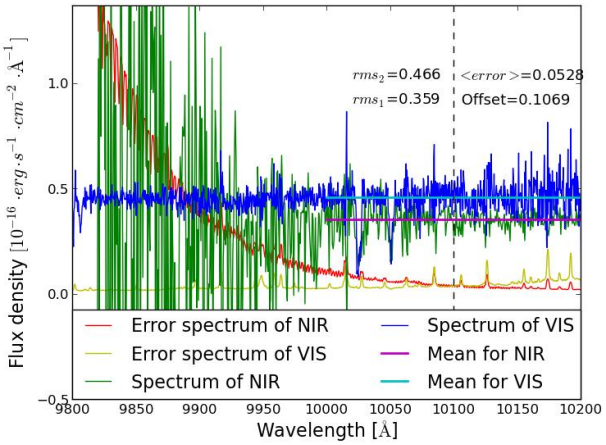

Fig. 9.— The original VIS and NIR spectrum before scaling and combination. Here rms_1 and rms_2 is the root mean square for VIS and NIR respectively for the spectral range marked.

NOTE: All the figures above are combination frames of the VIS and NIR for source nr 4. The black dashed vertical line marks the point, 10100 Å, where VIS and NIR is combined.

3.2.2. Continuum Fitting

After having sorted the spectra and performed the combination of VIS and NIR, the next step was to fit the continuum and perform the continuum subtraction. Hence a continuum fit was needed which was created by fitting a power law function to the "continuum windows" for each of the sources. A "continuum window" is a range of the spectrum with no or only few very weak lines. It is important to have continuum windows pretty evenly spread out over the whole spectrum in order to fit the overall shape of the continuum. The continuum regions are listed in table 3 as rest wavelengths. In the sample all the QSO spectra contained the continuum windows A-D and half the QSO spectra also included E and F.

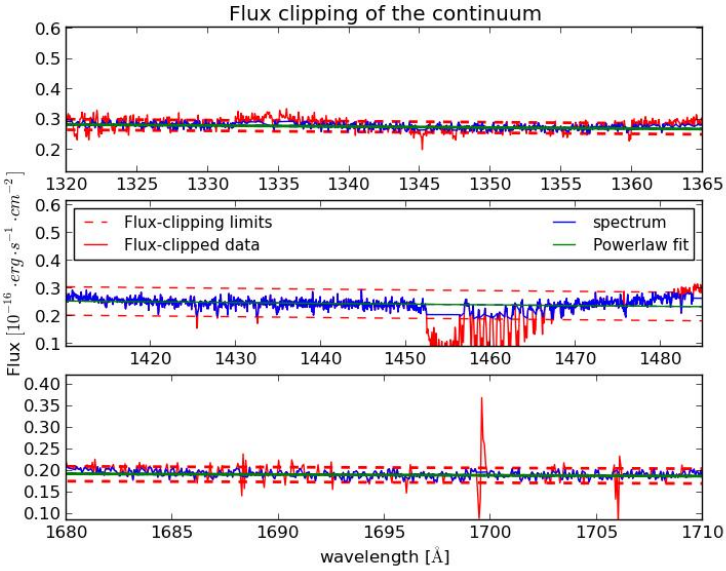

Fig. 10.— An example where flux clipping has been applied. The red lines show a 2.5σ deviation from the fitted power law and it proves necessary in the middle figure where some absorption can be seen.

The continuum of a QSO is consistent with a power law, which was used in the fitting routine. De Rosa et al. (2011) have determined the median value for the power to be -1.5 ± 1.2, for a survey of highly redshifted QSOs. Shen et al. (2011) investigated a sample of 100.000 SDSS QSOs at z<4.95 and found the mean value of the local slope around MgII to be -1.3. I used this value for the initial guess of the power in the chi-squared fitting routine when fitting the continuum. The continuum fit was created from the VIS and NIR combined spectrum. In order to avoid absorption lines or strong line wings influencing the continuum models flux clipping is applied and the continuum model was refitted. This was important because if there was absorption the continuum

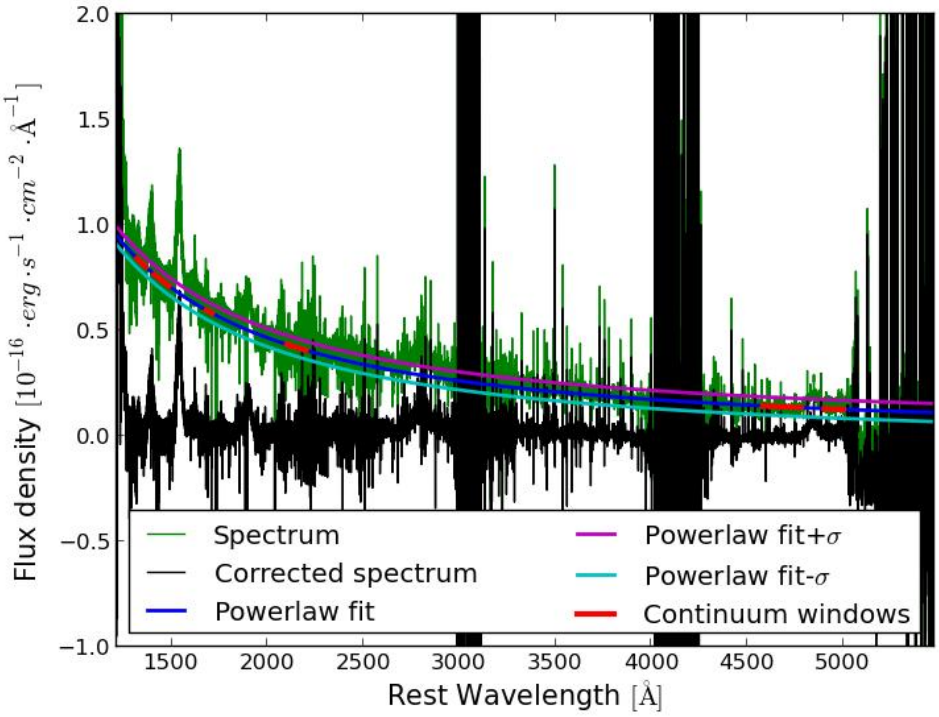

Fig. 11.— The continuum fit for source #4 where the green is the original spectrum and the black is the continuum subtracted spectrum. The red lines are the flux clipped continuum windows used for the continuum fit. The blue lines are in the centre the power law fit and the lines on each side are ± sigma indicating the uncertainty of the continuum fit. The very strong fluxes around 3000 Å, 4000 Å and 5000 Å are corrected telluric absorption bands. At some points the absorption is so strong that large uncertainties arise in the corrected flux values, which happens when small fluxes are corrected to the expected level of the non-absorbed spectrum.

model could be underestimated and if the model was affected by wings the continuum could be overestimated. An example of flux clipping can be seen in figure 10. After the flux clipping was done the fitting routine refitted the power law in order to obtain the final continuum fit used for the continuum subtraction.

For some of the sources the continuum fit was not a good representation of the overall continuum shape. Hence it was necessary to use different weights for each of the continuum windows. This meant that a continuum fitting window affected by e.g. a strong emission line wing should be weighted to be less important than the other windows. It was very typical for the high wavelength part of the spectra to have a

Table 3: Continuum Windows

Range	λ_{rest} Min[Å]	λ_{rest} Max[Å]
A	1320	1365
B	1410	1485
C	1680	1710
D	2100	2200
E	4580	4780
F	4900	5000

drop off in flux[9], this effect in some of the spectra coincided with window E and F. So in those cases their weights were set to zero. Other effects to look out for were strong absorption or emission lines and telluric lines, see figure 11. These different effects could mean that the continuum windows could become useless if the effect was too strong. A spectrum with such characteristics could still obtain a fit which was a good representation of the continuum shape if the weights for the affected regions were set correctly. An important thing to keep in mind when setting the weights is the overall shape of the whole continuum. It was not necessary to adjust the weights for most of the sources. In appendix A.3 the sources which needed the window weights set are listed.

When the continuum fit had been created, for the sources that needed the weighed continuum windows method, the next step was to estimate the uncertainty of the continuum fit. This was very important since the continuum uncertainty can be used as the upper threshold for the uncertainty of the emission line strength. It is necessary to have the uncertainty as it affects the measurements of the FWHM, σ_l and the line strength. The uncertainty of the power law model can be represented as:

$$\sigma_{\pm}^2 = \frac{1}{N} \cdot \sum_i (F_i - P_i)^2 \tag{11}$$

Here N is the total number of data points in the continuum ranges, i is each pixel or data point, F is the continuum flux and P is the power law model. Here note that this is done over the range of the continuum windows. Hence $\sigma_{\pm}$ will increase if the difference between the emission continuum and power law model is high. Using $\sigma_{\pm}$ makes sure that the possible misfit of the continuum is accounted for in the error estimation of the lines.

[9]This effect is caused by the detectors' absorption of light being less efficient at the edge of their ranges.

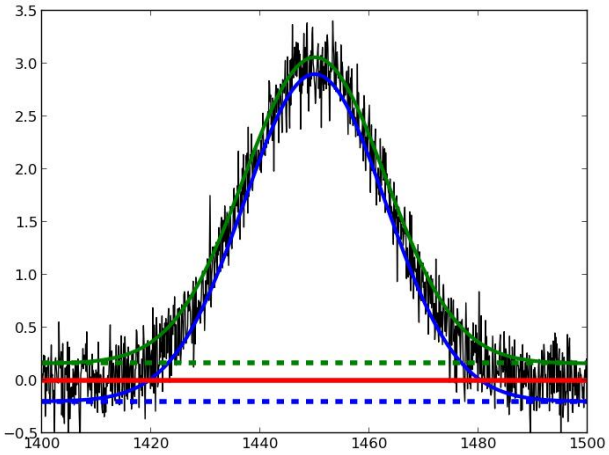

Fig. 12.— A representation of the possible error in the modelling of the BELs for an over- and underestimated continuum model. The black line represents an emission line with Gaussian distributed noise. The blue and green line is the model of the emission line when the continuum emission is under-or overestimated respectively. The blue and green dashed lines represents the boundary of the area the fit encloses i.e. the emission line strength. It is important to note that the y-axis would change the zero point for the two continuum models because the continuum is subtracted from the QSO spectra before creating models of the emission lines.

The importance of a good continuum fit can be seen in figure 12, here it is evident how the lines can be under- or overestimated if the continuum subtraction is bad. Here the problems could occur if we for example have a lot of absorption which is not a feature of the continuum itself but rather is an effect of intervening dust and gas clouds. The last thing to do was then to subtract the continuum from the spectrum (see figure 11), and use $\sigma_{\pm}$ to obtain the errors for each measured line. Here it is important to note that the uncertainty of the lines comes when σ_{-} is subtracted and σ_{+} is added in order to integrate over the whole line with the added or subtracted contributions respectively. This was done by integrating over the emission line profile $\pm\sigma_{\pm}$ using the same ranges as the emission line profiles.

3.2.3. Line Fitting

The next step towards determining the metallicity was to fit the BELs from Ly-α 1216 Å to CIII] 1909 Å, see table 4. As previously mentioned it was necessary to fit the lines as they are blended with each other. The BELs can also be affected by absorption which can be avoided by flux clipping, but for this a model of the line is needed.

Table 4: Emission line list

Line	Peak position [Å]
Ly-α*	1215.67
NV	1240.15
$NIV]$	1486.50
CIV	1549.05
$HeII$	1640.42
$OIII]$	1664.15
$NIII]$	1750.46
$SiII$*	1892.03
$CIII]$	1908.73

NOTE: This table shows all the fitted lines where * marks the lines that are only fitted because they are blended with one of the lines of interest, either NV or CIII].

Since the lines are blending it was necessary to create a model which could be used to fit the strong and most blended lines: Ly-α-NV and SiII-CIII]. For this a CIV template was created since its velocity profile is similar to that of the two complexes, and the weak lines NIV] and HeII (Korista et al. 1997; Dietrich et al. 2003b). This is explained in the sections below where the creation of the CIV-template is first explained thereafter the application of the CIV-template is explained for the two complexes and for the remaining weak lines.

3.2.3.1. Creation of the CIV Template

The CIV-template was created using three Gaussian functions following the methodology of Dietrich et al. (2003b,a,d). This was done in order to have a better basis of comparison between my observation and theirs.

The procedure of obtaining the CIV-template was as follows: Firstly a temporary model was created for the CIV emission line. The temporary model was then used to perform flux clipping around the CIV emission line in order to avoid disruptive absorption lines. The CIV temporary model was thereafter used to fit the weaker lines around CIV, NIV] & HeII. Here note that OIII] was fitted using two Gaussian functions. The weaker lines were then subtracted from the spectrum in order to create a continuum region on both sides of the CIV line. When the region around CIV had been cleaned of absorption and the weaker BELs the final CIV-template could be created.

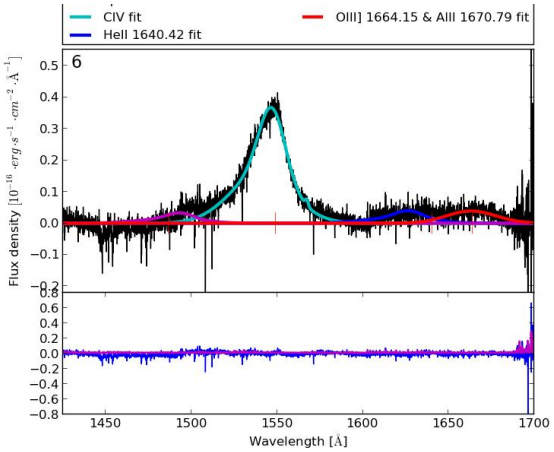

Fig. 13.— The fit of the CIV region with all the weaker lines present, the fit is of QSO J1033-0327 (#6)and the residuals, blue, are represented below the plot itself where the magenta shows the error spectrum.

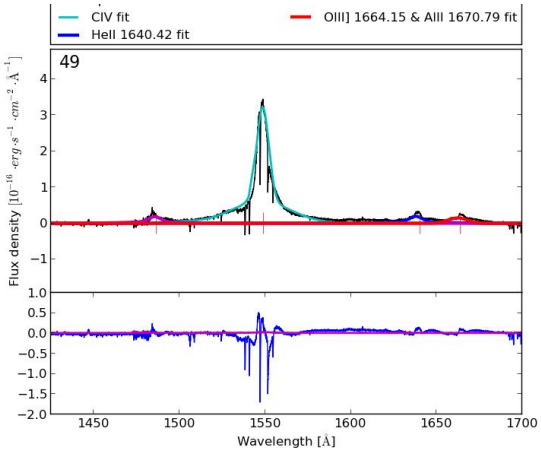

Fig. 14.— The fit of the CIV region with all the weaker lines present, the fit is of QSO BR 2248-1242 (#49) and the residuals, blue, are represented below the plot itself where the magenta shows the error spectrum.

It was crucial to obtain CIV-templates that were accurate representations of the line profile since the template was used to fit other lines. Hence an error in the CIV-template would affect all the BELs but OIII] and NIII] as these two lines were fitted using two Gaussian functions as opposed to using the CIV-template. A plot of a fit of all the lines can be seen in figure 13. Here it is clear that the NIV line is partly blended with the wing of CIV which makes this particular line very elusive because it is weak, around 5 % the strength of CIV (Dietrich et al. 2003b). It can be difficult to fit a very sharply peaked profile such as the one seen in figure 14. This would require additional Gaussian functions. The missed line flux is estimated to be low in comparison to the total line flux. The effect of missing some of the flux is estimated in section 3.2.5.2. This template was then used to fit the weaker lines around CIV (exept OIII]) and to model the Ly-α-NV- and SiII-NIII]-complexes, as described below.

3.2.3.2. Application

In this section the application of the CIV-template is explained: firstly for the complexes Ly-α-NV & SiII-CIII] and secondly for the weak lines NIV], HeII, OIII] & NIII]. Here it is again noted that the weak lines OIII] & NIII] are fitted using two Gaussian functions This is done in order to follow the methodology of Dietrich et al. (2003b) and since the velocity profile of OIII] & NIII] does not match that of CIV

according to Korista et al. (1997). In order to use the CIV-template as a model for the remaining BELs their respective velocity profiles are assumed to be similar to that of the CIV emission line. The reason why the CIV-profile can be used as a template is because the BELs have similar velocity fields since the lines are formed in the same region as CIV or close thereto (Korista et al. 1997). The CIV emission line is also very strong and not affected by other strong intervening emission lines which makes the creation of a template possible.

The QSO spectra did not include all the BELs that could be used for metallicity estimation. Hence before creating the fits the sources were sorted into five different groups (see table in appendix A.2). This was primarily done for practical reasons since the fitting routine would still try to fit a line even if it was clearly not present in the spectrum. The created groups turned out to have some characteristics such as for group I which typically had narrow lines and for group II the lines were generally broader (see appendix A.2).

The Line Complexes of Ly-α-NV & SiII-CIII]

The fit to the two complexes Ly-α-NV and SiII-CIII] had to be performed in a combined procedure as the lines were so severely blended. Generally there was much more work to be done for the Ly-α-NV complex which will be elaborated below. But first the fitting of the SiII-CIII] complex is briefly explained.

The SiII and CIII] emission line complex was often affected by noise since it was in the region close to the edge of VIS and NIR. Hence in some cases this made it difficult to fit the line complex. It was also clear that for some sources the SiII and CIII] had different velocity profiles than the CIV-template. This meant that fitting the CIV-profile was a bad representation of the shape of the complex, see figure 16. This should be expected because CIII] is an intercombination line and not a high ionization line such as CIV, this difference in their profiles have been predicted by Korista et al. (1997) which was mentioned in section 2.2.1. But for the majority of the lines the fit was a great representation of the line shape,see figure 17, supporting the theory that the CIV-template can indeed be used as a template for both SiII and CIII].

One of the challenges for the Ly-α-NV complex was the Ly-α forest which in some cases intervened with the Ly-α emission line absorbing it partially or in a few cases completely. The Ly-α forest intervened because of the high redshift of the QSOs in the survey. In some cases the NV emission line was also affected by prominent absorption

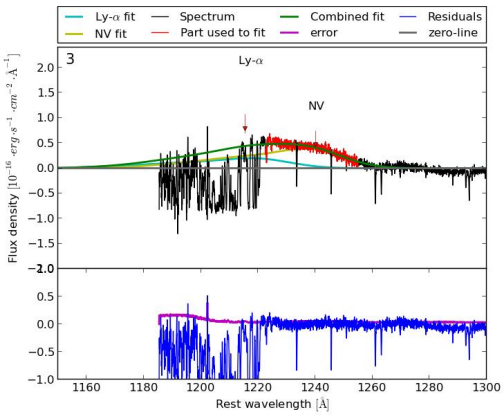

Fig. 15.— The fit of the Ly-α-NV complex of source #3. The lower panel shows the residuals when the model fit to Ly-α and NV is subtractedfrom the spectrum.

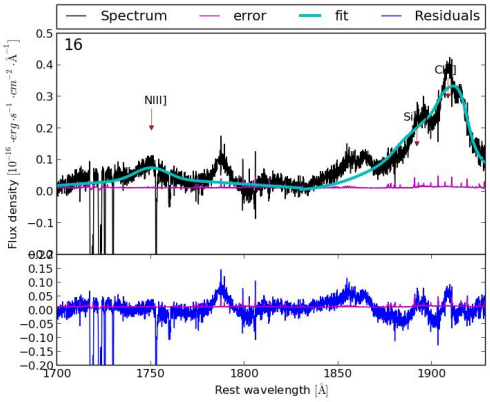

Fig. 16.— The fit to NIII], and the SiII and CIII]-complex modelled for source #16. The lower panel shows the residuals when the model fit to NIII], and the SiII and CIII]-complex is subtracted from the spectrum.

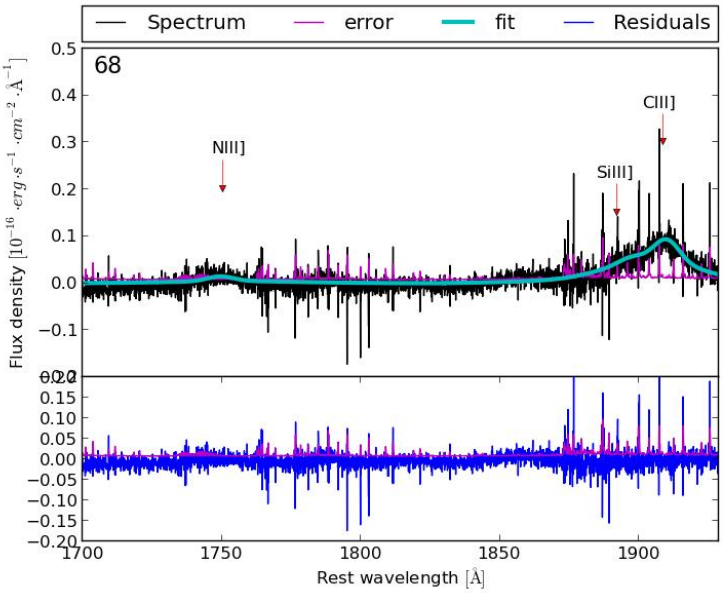

Fig. 17.— A typical modelling to NIII] and CIII] for source #68.

lines which made it difficult to fit the line. The worst case of a grossly underestimated Ly-α and NV-line can be seen in figure 18. For this profile it is evident that it is the combination of a lot of broad absorption lines that makes the complex impossible to model. The reason why the broad lines pose such a problem is because they contain more data points than the narrow lines. Therefore the broad lines affect the fitting

procedure more than the narrow lines. But for most of the sources it was possible to create good representations of the emission line complex by clipping the absorption lines from the spectrum. This was done manually, in the sense that I had to read from the Ly-α-NV plot where absorption lines started and ended. This can be seen in figure 18 where the red line is the part used by the fitting routine to create the fit.

Luckily this is the worst fit and does not represent the general trend for the Ly-α and NV fits. A typical fit of the Ly-α and NV complex can be seen in figure 19. One of the typical problems was to get the topmost part of the Ly-α line fitted (see figure 19). But as it is the NV line we are most interested in this is still a good representation of the NV emission line profile. There was another issue with the lines other than strong absorption. In some cases the Ly-α and NV-line complex was so severely blended that it was hard to distinguish the two lines. This is a serious problem with no method to solve it. For most of the cases the fits of the severely blended lines were excellent, see figure 15. But if this is because the velocity profiles actually match or if it is simply because it is easier to fit a broad stubby and blended line than a sharply peaked profile with distinctive characteristics is unclear. It may however be unwise to put to much trust in the metallicity estimates from the heavily blended complexes and therefore they will be flagged in further sections to make sure we remember this.

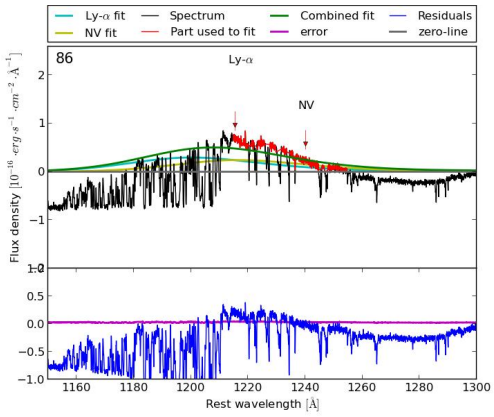

Fig. 18.— The worst fit to Ly-α and NV was source #86. The residuals of the fit can be seen in the lower panel.

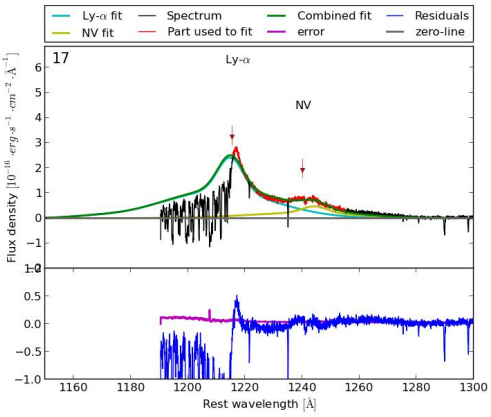

Fig. 19.— The fit of the Ly-α-NV complex of source #17. This is a nice but representative fit of a complex without to many absorption lines and where there is a rather clear distinction of the two lines.

The Weak Lines NIV], HeII, OIII] & NIII]

The remaining emission lines I needed to fit were NIV], HeII, OIII] & NIII]. Here OIII] and NIII] were fitted using two Gaussian functions and the rest were fitted using the CIV-template.

The lines in the region around CIV were first fitted after the CIV-profile had been subtracted. Then it was relatively easy to fit NIV] if it was present. The two remaining lines were a little more complicated as they were relatively close to each other which meant that they were often blended. This was resolved by fitting them simultaneously in the same manner as the complexes above, but here OIII] was fitted using only two Gaussian functions. The OIII] line was often quite weak so in some cases it was unclear if there was an emission line or if it was simply noise. It was noted that the range in the spectrum around OIII] was generally noisier than the range around HeII.

The last line to fit was NIII] which was also fitted using two Gaussian functions. This line was often very weak and could be disturbed by emission lines in the region between NIII] and SiII. This was not helped by the fact that this part of the spectrum was noisier than for the lines at lower redshift The profiles for all the BELs present was however recovered and the fits are in general good representations of the emission lines.

3.2.4. Determining the Line Strengths

When all the lines had been fitted the line strengths for the individual lines were determined. This could be done in two different ways. Either the line strength could be obtained by simply integrating over the fitted profile, or by integrating over the spectrum using the fit to obtain appropriate integrational limits. There are pros and cons for each of the methods which will be discussed in this section.

For a perfectly fitted line the fit should in theory be a better representation of the emission line because the observation only spans over a relatively short period of time. But if the fit is not perfect the line strength will be over- or underestimated. The advantage of using the second method is that it will include all the bumps and shoulders of the lines that a Gaussian fit could potentially miss. But on the other hand integrating over the spectrum could add contributions from absorption lines, noise and possibly other emission lines since most of the BELs are intervening. In order to measure the complexes it would be necessary to subtract the fit of the secondary

line from the spectrum before integrating over the spectrum. So for e.g. the Ly-α-NV complex the fit to Ly-α would be subtracted whereafter the spectrum would be integrated over a proper range. Therefore this method would still be model dependent if we had to use it for the complexes. But since the intervening lines and complexes require model fits it is best to use the fitting method in order to have line strengths that are comparable. Therefore the method of modelling the lines rather than integrating over the original spectrum was chosen.

Determining the emission line strength using the fitted models was straightforward. The line profile for each of the fits was integrated over all of the spectrum. The uncertainties of the emission lines were determined from the uncertainty of the continuum fit as previously mentioned using $\sigma_{\pm}$ from equation 11, where the uncertainty was added or subtracted from the model for the upper or lower limit respectively. Then the upper and lower limit of the model as well as the model itself was integrated in order to obtain the emission line strength along with the upper and lower uncertainties. The objective was to determine the metallicity which was earlier explained to scale with specific emission line ratios presented in section 2.2.1 where the determination of the metallicity is explained in the next section.

3.2.5. Metallicity Determination

When the line strengths had been measured they were first transformed into the line strength ratios and then into the metallicity using the conversion functions shown in figure 6. In this step the errors, $\sigma_{\pm}$, were computed as follows, using the line ratio $\frac{NIII]}{CIII]}$ as an example:

$$\sigma_{\frac{\text{NIII]}}{\text{CIII]}}} = \sqrt{\left(\frac{\sigma_{\text{NIII]}}}{L_{\text{CIII]}}}\right)^2 + \left(\frac{\sigma_{\text{CIII]}} L_{\text{NIII]}}}{L^2_{\text{CIII]}}}\right)^2} \tag{12}$$

Here σ is the mean error, i.e. $\langle\sigma_{\pm}\rangle$, and L is the line strength where the subscripts specify the BEL in question which for this example is either NIII] or CIII]. The reason why the mean error is used rather than σ_+ and σ_- is mainly for simplicity and because the difference between the two is insignificant. The largest difference comparing σ_+ to σ_- show up on the 12th decimal. Hence within the precision of this study which is on the 8th decimal the two are equal.

3.2.5.1. Model Selection

When the metallicity and associated error had been determined from the emission line ratios, the next step is to use the scaling relations presented in section 2.2.1 (see figure 6) to obtain the metallicities. Using different continuum models to obtain the metallicities affect the final metallicity. Hence it is important to choose the continuum model which most accurately describes the continuum (see section 3.2.2). In section 2.2.1 I presented the three conversion models each with a different continuum model: the hard power law, the segmented power law and the empirical power law presented by Mathews & Ferland (1987).

The continuum model most consistent with our spectra is the hard power law since the mean power law slope of the sample is -1.426 $\pm$ 0.416. which is consistent with the results of (Shen et al. 2011; Decarli et al. 2010; De Rosa et al. 2011). Dietrich et al. (2003b) states that the segmented power law model was the most appropriate to use since this had been shown by Zheng et al. (1997). The sample Zheng et al. (1997) used consists of 101 QSOs with z>0.33, of which only 6 have a redshifts above 2. They use the part of the spectrum blueward of Ly-α which has a different continuum slope than the part of the continuum redward of Ly-α. But because the objects of the XQ-100 Legacy Survey have redshifts typically around 3 and higher the Ly-α forest completely absorbs the part of the spectrum blueward of the Ly-α line. Therefore it makes little sense to fit the continuum with any of the data in the Ly-α forest as it sets no real constraints on the continuum. Zheng et al. (1997) state that between 1050 Å and 2200 Å the continuum can be modelled as a power law with a slope of 0.99 $\pm$ 0.05. This range includes all the BELs necessary to determine the metallicity and therefore it makes sense that the hard continuum model should be used for this range. I check the consistency of the metallicity estimates based on the different continuum models for the line ratios: $\frac{NV}{CIV}$ and $\frac{NV}{HeII}$. I found that the hard power law model provided metallicity estimates for the two line ratios which were consistent with each other (see figure 22) which the segmented power law did not (see figure in appendix D). Hence I have chosen to use the hard power law to convert the emission line ratios into the metallicity, rather than the segmented power law used by Dietrich et al. (2003b).

The metallicity estimates I obtained are represented in figure 20. Here the overall level is super-solar in accordance with the expectations (see section 2.2). From the figure it can be seen that the highest metallicity estimates are obtained for $\frac{NV}{HeII}$ which have metallicity estimates as high as $30Z_{\odot}$. The other line ratios provide metallicities in the range of $\sim$ 1-5 $Z_{\odot}$. In figure 21 the metallicity estimates, obtained by Dietrich et al. (2003b), for the same line ratios as I have used are presented. My estimates

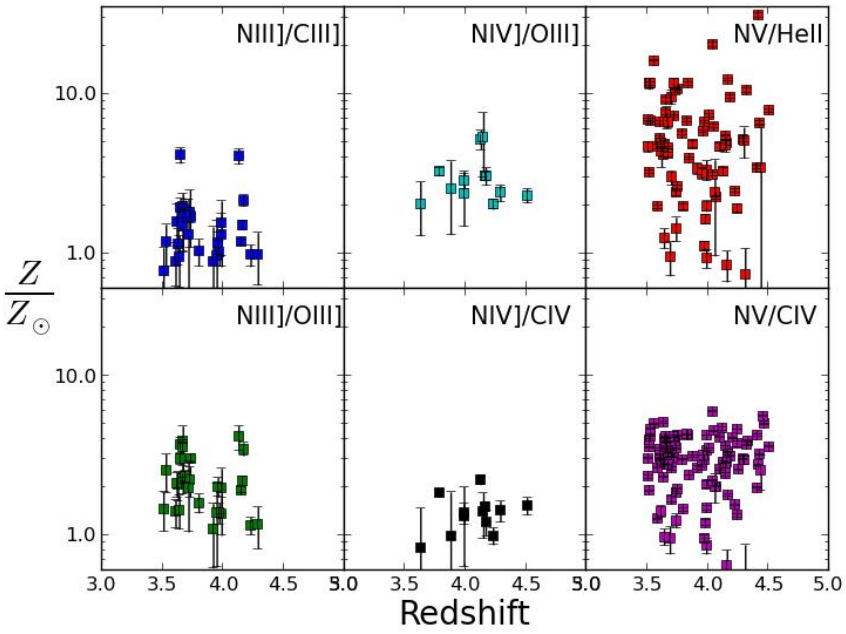

Fig. 20.— The metallicity estimates for the different line ratios obtained in this thesis in the same manner as those estimates shown in figure 21.

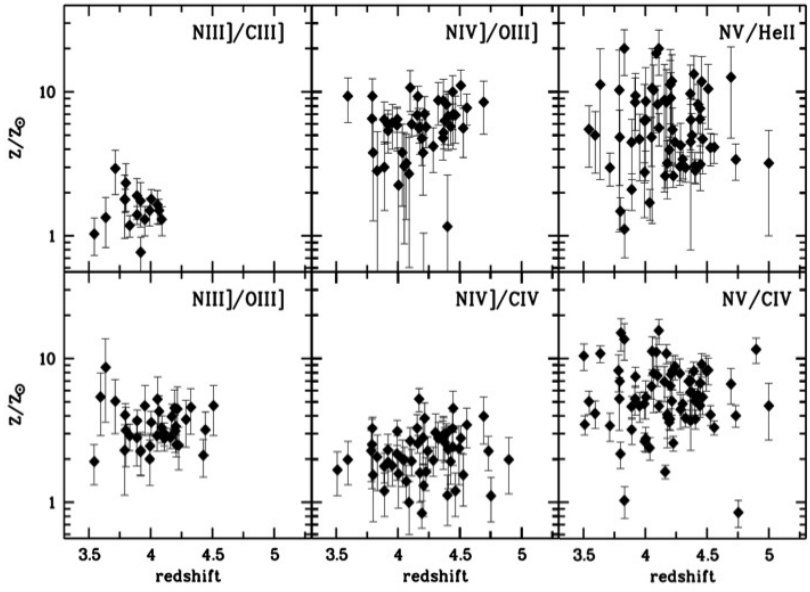

Fig. 21.— This figure is taken from Dietrich et al. (2003b) (figure 2) where the plots showing the ratios involving OVI have been removed.

are clearly consistent with those of Dietrich et al. (2003b). The overall trend of how the metallicity estimates scatter for the different line ratios look very similar. But the numerical values of my metallicity estimates are generally lower. One reason for this may be that Dietrich et al. (2003b) overestimated the N emission line strengths, but this will be elaborated further in section 4.

By comparing the metallicities obtained from the different line ratios we may uncover potential effects that are important to account for in the current analysis. I expect that the metallicity obtained from one line ratio should be the same as that determined from another line ratio I would expect a rough 1-1 correlation between metallicity estimates i.e. $Z\left(\frac{NV}{CIV}\right) \sim Z\left(\frac{NV}{HeII}\right)$. In order to check if this is true I show all the possible combinations of comparisons between the metallicities obtained from the different line ratios (see appendix B.1). The diagrams show that the majority of the plots were simple scatter plots (see appendix C). This may indicate that not all of the scaling relations are suitable for metallicity estimates, which is discussed in section 5.

In figure 22 the metallicities from $\frac{NV}{CIV}$ and $\frac{NV}{HeII}$ are compared. In the plot there is a strong 1-1 correlation up to a metallicity of around 3 whereafter the metallicity rises more for $\frac{NV}{HeII}$ than for $\frac{NV}{CIV}$. In order to asses the cause of the offset the fits were visually inspected. The possible explanation for the offset could be that the determination of the line strengths are associated with systematic errors for either HeII or NV. The reason why CIV is not considered to cause this is because the modelling of CIV have been accurate and had a low uncertainty on the emission line strength. I firstly investigated the modelling of the HeII emission lines. I found that the models for HeII very accurate representations of the emission line and had reasonable uncertainties, which were typically lower than 25% of the emission line strengths. Then I investigated the NV emission lines where I noticed that many of the sources had severely blended Ly-α-NV complexes and in some cases the Ly-α emission line was completely consumed by the Ly-α forest. In these cases the determination of the NV emission line is a problem. For the case with a severely blended complex it is not possible to know if the fitted profile of NV is correct, since there is no telling what part of the complex makes up the NV emission line. These profiles may very well be perfectly fitted, which they in fact in the most cases are, but only if we can make sure that the velocity profiles are the same we can put any trust into these complexes, and this is not possible. For the complexes with an absent Ly-α emission line the estimation of NV was also uncertain as there was no constraint on the Ly-α profile which could affect the fit of NV.

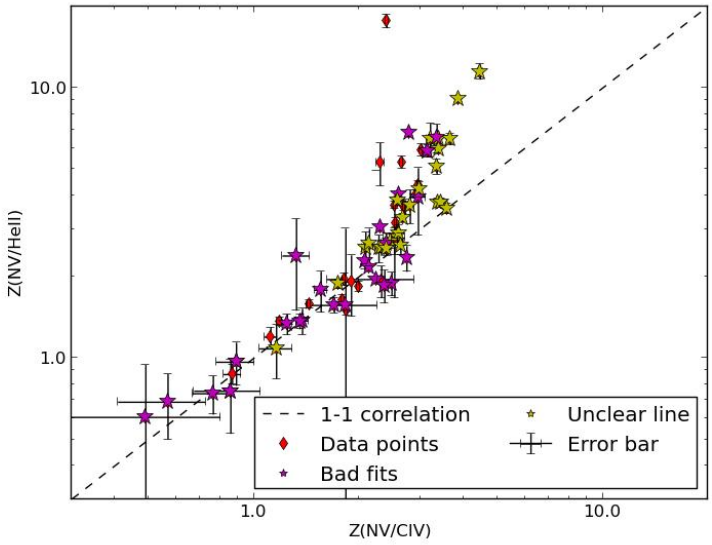

Fig. 22.— The comparison of the metallicity obtained from two different line ratios. The yellow stars mark the sources where the lines was blended or if the Ly-α line was engulfed by the Ly-α forest. The magenta stars show the sources with bad fits to NV, these data points should not be disregarded but in reality have larger uncertainties ascribed. In the legend unclear line means when the Ly-α-NV emission lines are severely blended and bad fits is the non-optimal fits discussed in the main text.

Therefore the sources with these complexes should not be relied upon and the results were marked with a yellow star in figure 22. When we look at the figure the yellow stars are spread quite evenly out with a slight overweight of yellow stars at the offset. But there are still too many data points with the offset so it cannot only be explained by uncertain estimates of NV. As I inspected the Ly-α-NV complex I noticed that there were non-optimal model fits for the complex. These may contribute to the offset so I investigate the effect of this in the next section.

3.2.5.2. The effect of non-optimal model fits of NV

The non-optimal model fits of the Ly-α-NV complexes are a result of the velocity profiles of CIV being different from the velocity profiles of Ly-α and NV. For the complexes with non-optimal model fits it was easy to estimate how much flux was missed by looking at the residuals and then integrating over the range at which the NV-residuals were at, see figure 23. The missed flux was then added to the emission line strength of NV in order to obtain a new metallicity estimate. Thereafter the difference in the metallicity between the model of NV and the combined contribution

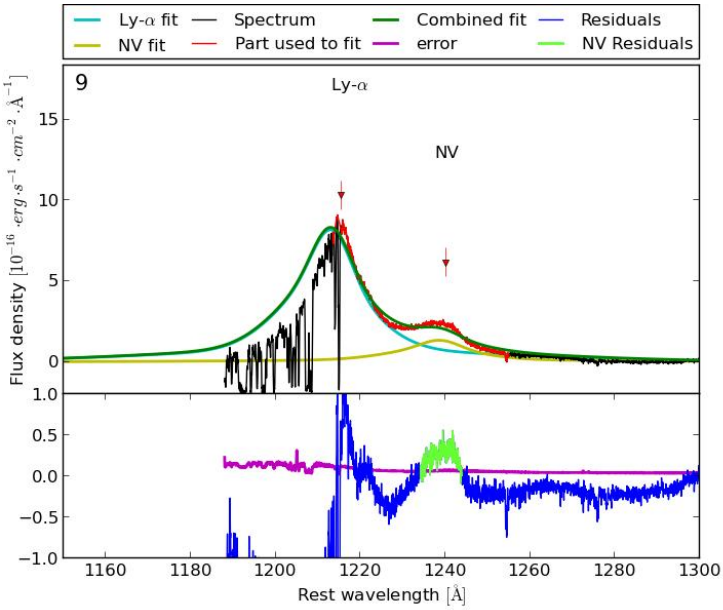

Fig. 23.— A non-optimal fit of source #9. Here the yellow-green line in the lower panel indicates the region over which the NV-residuals were integrated. This was done in order to estimate how much of the NV line was missed by the model.

from the model and the missed fit was determined. This was done for the 26 worst fits which are presented in table **??**. The effect of the underestimation of the lines can be seen in figure 24 and 25. Here it is seen that the general underestimation of NV leads to an additional error of 0.3 $Z_\odot$ for $Z\left(\frac{NV}{CIV}\right)$ and 1.3 $Z_\odot$ for $Z\left(\frac{NV}{HeII}\right)$. These values are within 10 % of the original estimate so the bad fits are still valid to use as long as extra error bars are added, this could be done as a precaution for all the metallicity estimates of $\frac{NV}{CIV}$ and $\frac{NV}{HeII}$ in order to make sure that the actual error is not underestimated. Adding the error would also be appropriate since the error we have now does not account for the uncertainties from the emission line modelling itself.

It is comforting to see that a non-optimal model does not have a huge influence on the metallicity (see figures 24 and 25). The main issue measuring NV is therefore not the possibly different velocity profiles leading to non-optimal fits but rather the severely blended Ly-α and NV-complexes. It is obvious to check whether the sources with severely blended lines are in a special group of QSOs. Because I do not want to reject a distinct group as this would introduce a selection bias in our sample. If it is true that high mass and redshift put a constraint on the reliability of the current methods it would be optimal to find a new method for obtaining the metallicity estimates. But when we see the result from the flagging the yellow stars are widely spread over the whole range and thus does not indicate that this group is characteristic (see figure 22).

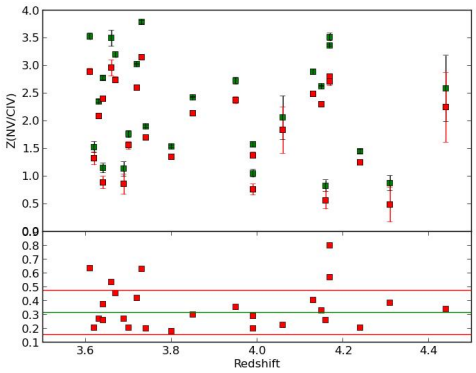

Fig. 24.— The effect non-optimal models has on the metallicity estimates for $\frac{NV}{CIV}$. Here the difference is caused by the non-optimal model can be seen in the bottom panel. The red squares in the upper panel indicates the original measurements and the green squares indicates the measurements with the added contribution from the integration over the NV residuals i.e. the missed part from the non-optimal fit.

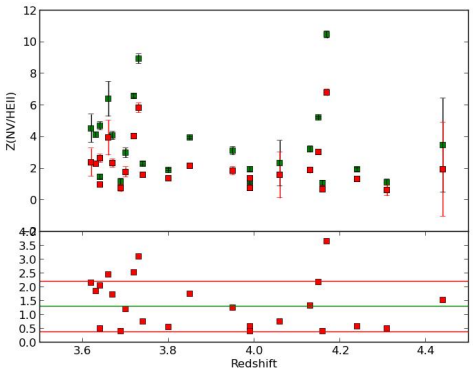

Fig. 25.— The effect non-optimal fits has on the metallicity estimates for $\frac{NV}{HeII}$. Here the difference is caused by the non-optimal model can be seen in the bottom panel. The red squares in the upper panel indicates the original measurements and the green squares indicates the measurements with the added contribution from the integration over the NV residuals i.e. the missed part from the non-optimal fit.

The flagged sources come from all the groups with a slightly higher percentage for group II which is primarily due to lower S/N than the other groups. The possibility of a severely blended Ly-α-NV complex rises with broader emission lines, as broader lines easier blend. There is a correlation between the width of CIV and the mass, which was the template used for fitting Ly-α and NV, so if the group of flagged lines are severely blended because of their widths correlating with their masses this must be possible to see when we look at how the masses correlate with e.g. the metallicities. But this was not seen, this must be due to the fact that the SMBH mass also depends on the flux level of the continuum. Some of the sources were flagged because the Ly-α forest completely engulfed the Ly-α so there were no constraints on Ly-α. This only happens at high enough redshift so if the mass-redshift-distribution of the sources shows that the flagged sources are of high mass and metallicity these must be the primary indicators of the group with severely blended lines.

In order to explain the offset from the 1-1 correlation noted in figure 22 I investigate other possible explanations. The rise is still prominent after having flagged all the severely blended lines, yellow stars, and all the non-optimal models of NV. Hence the

offset cannot be explained by non-optimal fits or severely blended lines. There seem to be two possible explanations for the rise from the 1-1 correlation. One possibility is that $\frac{NV}{HeII}$ does not scale with the metallicity for high metallicities. This has already been shown by Hamann & Ferland (1993b) who found that the flux for the $\frac{NV}{HeII}$-ratio decreases with higher density and flux. It was again mentioned by Hamann & Ferland (1999) that the maximum value of the $\frac{NV}{HeII}$-ratio was around $\sim$ 2-3 which would correspond to metallicities higher than 3 $Z_{\odot}$. This is beyond the range of the measured metallicity so another explanation for the offset is necessary Another possibility could be over-excitation of HeII in the BLR. If over-excitation happens in some regions of the BLR the HeII emission line flux would be lower than if there was no over-excitation. Over-excitation of the gas is most likely to happen in the BLR gas closest to the SMBH as this is the region of the BLR with the highest energy. But both explanations may be the cause of the rise of the metallicity estimate from the 1-1 correlation.

The offset can also be seen in the data from Dietrich et al. (2003b) but they do not comment on it. Not having seen how they are fitting the data some of the offset points could very well be due to severely blended Ly-α-NV emission line complexes, which do have a tendency to have high estimations of NV.

3.2.5.3. Offset Calibration

When I examined the other plots comparing the metallicity estimates from the different ratios I noted that there was an offset for $\frac{NIII]}{OIII]}$ vs. $\frac{NIII]}{CIII]}$ and $\frac{NIII]}{OIII]}$ vs. $\frac{NIV]}{CIV}$, see figures 26 and 28.

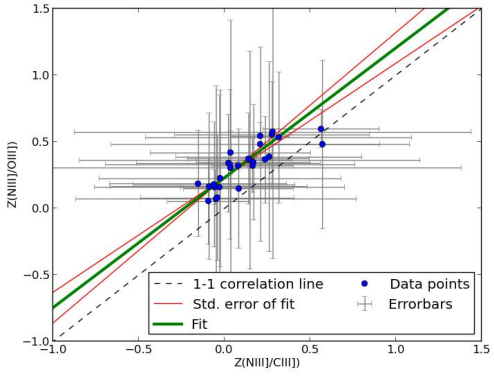

Fig. 26.— The offset in metallicity of $\frac{NIII]}{OIII]}$ in comparison to $\frac{NIII]}{CIII]}$ and the fit to the data.

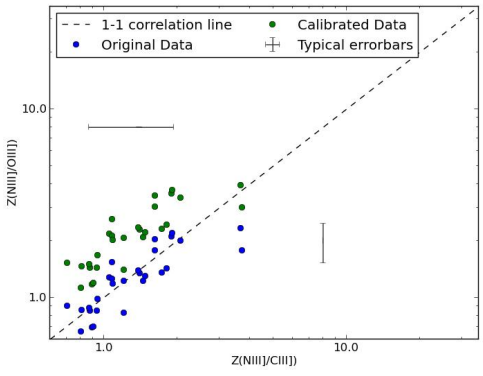

Fig. 27.— The originally offset data points and show the result of the recalibration.

For $\frac{NIII]}{OIII]}$ vs. $\frac{NIII]}{CIII]}$ it was clear that there had been a systematic underestimation of OIII] which was consistent with the spectra and with the fact that in the region just around OIII] there was often a lot of noise or absorption. Therefore I chose to calibrate $\frac{NIII]}{OIII]}$ which was done by first fitting a straight line to the data points and then subtracting the zero point offset of the fitted line from the 1-1 correlation for $Z\left(\frac{NIII]}{OIII]}\right)$. The slope for the fitted line was 0.976 ± 0.115 which was consistent with the slope of the 1-1 correlation (a slope of 1). Hence the metallicity estimate from $Z\left(\frac{NIII]}{OIII]}\right)$ was subtracted from the offset of the fitted straight line, which was 1.70 $Z_{\odot}$, which provided the calibrated metallicities seen in figure 27.

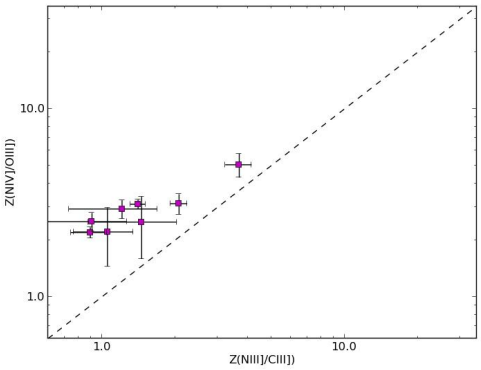

Fig. 28.— The offset in metallicity of $\frac{NIII]}{CIII]}$ in comparison to $\frac{NIV]}{OIII]}$.

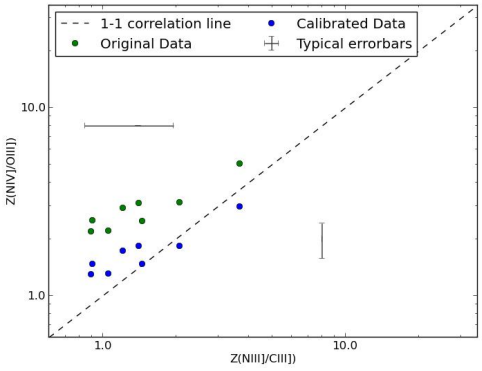

Fig. 29.— The result of the recalibration of $Z\left(\frac{NIV]}{OIII]}\right)$.

Now for the plot comparing $Z\left(\frac{NIII]}{CIII]}\right)$ to $Z\left(\frac{NIV]}{OIII}\right)$ in figure 28 there were only 8 data points so fitting them and using the fit to recalibrate the data was an unreliable method. Therefore the offset subtracted from the other figure was used as it was deemed that the offset was caused by underestimation of OIII] which was also present in the second line ratio. The offset of the line was 0.230 ± 0.017 this was subtracted from $Z\left(\frac{NIV]}{OIII]}\right)$ and the results can be seen in figure 29. For these calibrations it should be noted that the error of the line should be added in the error of the metallicity estimate as the calibration itself introduces these errors.

3.2.5.4. Combination of the Metallicity Estimates

So after having converted the line ratios into metallicities using the most appropriate continuum model (the hard power law) and having calibrated the offset for $\frac{NIII}{CIII}$ and $\frac{NIV}{OIII}$ I could finally combine the metallicities from the different emission line ratios. This can be done using two different methods.

Dietrich et al. (2003b) have simply taken the average of the metallicity estimates and for simplicity this may be the best approach. I investigated the option of weighting the individual metallicity measurements for the final metallicity estimate for each QSO. It is not obvious how to weight each measurement. I experimented with the following weighting schemes: inverse variance weighting and basing the weights on the line ratios on how well they can estimate the metallicity based on observations and theory. For inverse variance weighting the normalized inverse variance of the metallicity estimate is used for each line ratio to determine the weight associated with each of the measurements, where the normalization means that the inverse variance is divided with the number of emission line ratios used so for e.g. group II this would be two. This means that if a metallicity estimate have a high uncertainty it will be weighted lower. The last method requires setting the weights, hence I have created a table that shows the weights associated with each of the ratios, see table 5. This was done in order to make it less subjective and more objective since comparing the line ratios to each other includes some level of subjectiveness.

I found that the error weighed average give final metallicity estimates higher than the listing weighted average, see figure 30. All the metallicity estimates from the different line ratios are within 1 σ and thus the method of combining the metallicity

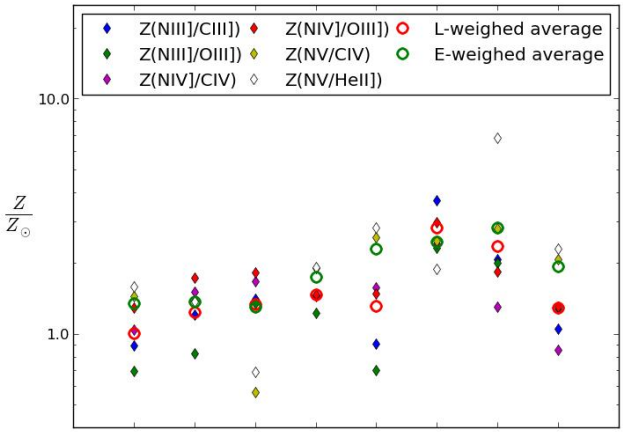

Fig. 30.— The metallicity estimates from the different line ratios and the average weights for group I. The weights are either dependent on the error of each of the line ratios or dependent on the listing seen in table 5. Note the x-axis does not have a caption because it is just a way to show each of the objects with equally separated spaces.

Table 5: This table shows the listing of the different line ratios. The listing is used to combine the metallicity estimates and the combined weights in the table are an estimate of how well an emission line ratio estimates the metallicity taking observation and theory into account.

Metallicity Tracer	Visibility
$\frac{NV}{CIV}$	$\frac{NV}{CIV}$
$\frac{NIII]}{OIII]}$	NIII/CIII]
NIV]/OIII]	$\frac{NV}{HeII}$
$\frac{NIII]}{CIII]}$	NIV]/CIV
NIV/CIV	$\frac{NIII]}{OIII]}$
$\frac{NV}{HeII}$	$\frac{NIV]}{OIII]}$

Combined Listing	Weight
$\frac{NV}{CIV}$	2.0
$\frac{NIII]}{CIII]}$	1.5
$\frac{NIII]}{OIII]}$	1.0
$\frac{NIV]}{OIII]}$ NIV]/CIV $\frac{NV}{HeII}$	0.5

estimates does not affect the end result significantly. Therefore I have chosen to combine the metallicity estimates from the different ratios using inverse variance weighting as there is no clear advantage of using the more complicated method.

3.2.6. $\frac{FeII}{MgII}$ Determination

In this section the methods for obtaining the $\frac{FeII}{MgII}$-ratio is briefly explained. The actual data processing has been performed by M. Vestergaard and figure 31 in this subsection is created by her.

The $\frac{FeII}{MgII}$-ratio is based on the emission line strength of the FeII pseudo-continuum and the MgII 2798 Å & 2803 Å doublet. In order to measure the emission line strength the spectrum was fitted using a model consisting of a power law continuum and emission of an empirical template of AGN FeII emission. The template was created by Vestergaard & Wilkes (2001) on the basis of an FeII emission spectrum of the nearby AGN I Zwicky 1 (IZw1). This object exhibits strong FeII emission and have relatively narrow BELs with a velocity dispersion around 900 km·s^{-1}. The reason why this object has been chosen as a template for the FeII emission spectra is because it has relatively narrow BELs. This makes it possible to use the FeII template from IZw1 for other AGNs with a range of line widths, from the lowest measured ∼900-1000 km·s^{-1} to the highest (∼15000 km·s^{-1}). When the template is modelled to a QSO with broader lines the spectrum of the template is broadened by folding it with a broadening profile, e.g. a Gaussian function, in order to simulate a broadening of the BELs in accordance with the BELs present in the spectrum. The reason why an AGN with relatively narrow

BELs has been chosen is because it is easier to broaden a line than to deconvolve it.

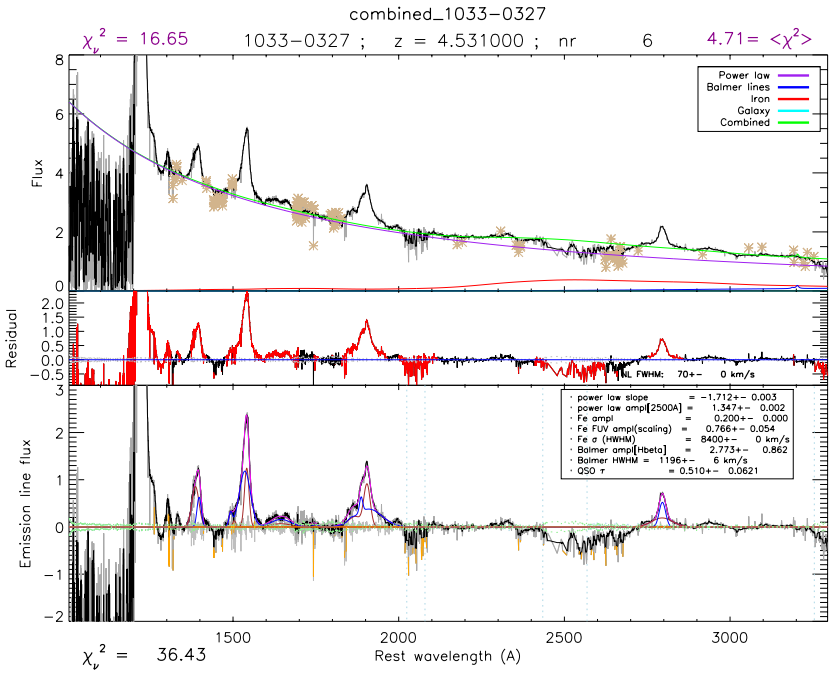

Fig. 31.— The modelfit created by M. Vestergaard to the FeII pseudo-continuum, MgII doublet, and the remaining BELs for #6. where the beige crosses marks where flux clipping has been applied. Flux clipping was used if there were narrow strong absorption lines in the spectrum. The two Gaussian functions modelled to the BELs are shown with the blue and brown curves, respectively where the combined emission line fit is in magenta.

The FeII template was fitted to the spectrum in specified energy ranges, much in the same way the continua were fitted to continuum windows in section 3.2.2. The fitting routine used to obtain the correct model parameters was the Levenberg-Marquardt Least-squares optimization as implemented in IDL. An example of the result is presented in figure 31. The FeII emission line strength was measured as the integrated intensity over the iron model in the range between 2200-3090 Å, which is the same interval Dietrich & Hamann (2008) use. The line strength was measured on the model in order to avoid the effects of telluric absorption. M. Vestergaard found that the telluric absorption could suppress the FeII strength in and around the telluric band. Yet the telluric correction can sometimes also lead to higher intensities in the

bands than expected due to the uncertainties in the telluric corrections. The FeII and MgII was only measured for 86 sources because some of the MgII emission lines were affected by telluric absorption which made it impossible to measure.

After the continuum and FeII emission models were subtracted the model for the MgII emission lines was created using two Gaussian functions. Because MgII is a doublet two Gaussian functions were fitted to it at 2798 and 2803 Å. The BELs: CIV, NIV], HeII, AlIII & OIII were then fitted, where CIV, HeII, AlIII & OIII were fitted with two Gaussian functions and NIV] was fitted with one Gaussian function. In figure 31 it is the sum of the Gaussian functions that are seen if the lines lie close to each other in energy.

On the basis of the model the FWHM and line dispersion is measured. The monochromatic luminosity is measured from the power law model. I use these parameters in the next section to determine the mass based on the MgII and CIV emission lines, respectively. I then compare the estimated masses from CIV for my measurements and M. Vestergaard's measurements in order to see if there are any systematic errors we need to account for.

3.2.7. Mass Determination

In this section the method for obtaining the SMBH mass is explained. The masses are determined using equations 8 and 9 presented in section 2.3. The parameters measured was the FWHM and line dispersion, σ_l, for CIV and MgII respectively along with the flux level at 1350 Å and 2100 Å, where the measurements of MgII were provided by M. Vestergaard, who also measured CIV. I compare my measurements of CIV and the flux level with the measurements obtained by M. Vestergaard before combining the mass estimates (see section 2.3) in order to make sure that they are comparable. The reason why I have to do this is because we have modelled the emission lines differently and optimized the modelling of the continuum for two different regions.

Since the luminosity is required in equations 8 and 9 the measured flux levels were determined using the flux-luminosity relation in equation 4. This required the luminosity distance, d_l, which was determined using the Kempner Net Cosmology Calculator[10]. The calculator assumes a slightly different cosmology than the given

[10] *http://www.kempner.net/cosmic.php*

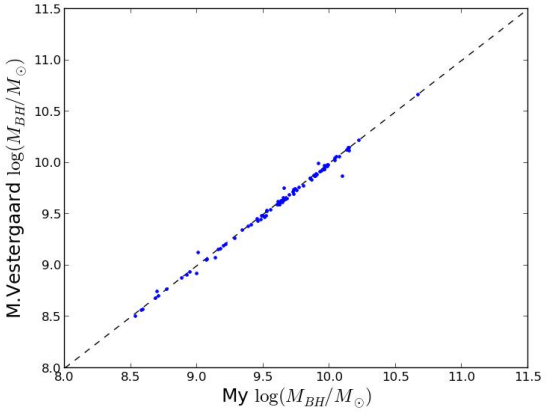

Fig. 32.— Comparison of the mass I obtained Vs. the mass obtained by M. Vestergaard for CIV. The stribed line indicates the 1-1 correlation line.

ΛCDM cosmology with $H_0 = 67.04$ km·s^{-1} Mpc^{-1}, $\Omega_M = 0.3183$ and $\Omega_\Lambda = 0.6817$ but this affects the mass estimates minimally (by adding ∼0.04 dex to the SMBH mass). The same cosmology was used by M. Vestergaard.

Before I could combine the two mass estimates based on MgII and CIV respectively I had to make sure that there were no offsets in our measurements indicating differences in our methodology and possibly non-optimal fits of the continuum. Hence I compared the mass estimates I had calculated for CIV with those determined (for CIV) by M. Vestergaard and I found that the majority were whitin the measurement uncertainties, see figure 32(see appendix E for the comparison of our flux levels). Therefore the mass estimates on the basis of MgII and CIV could now be combined.

When I had made sure the measurements were comparable I could finally combine the mass estimates based on CIV and MgII, which i did using inverse variance weighting, see section 3.2.5.4. The difference in the measurements of the mass based on CIV and MgII was within the uncertainties which was ∼0.4 dex. Here it is important to note that the mass estimates based on CIV are based on my measurements since I model the CIV emission line more accurately. This is because I use three Gaussian functions and have optimized my continuum model to this region where M. Vestergaard only uses two Gaussian functions and has optimized the continuum for the range from 2000-3000 Å. But the difference in our measurements is small, and the results primarily differs for the objects with very peaky profiles, since those profiles are especially hard to model, as previously mentioned in section 3.2.3.1 more Gaussian functions are preferable for this type of profile. The combined average mass estimate based on both MgII and CIV are presented in the next section.

4. Results

In this section I present the results of the data analysis. I have measured the line strengths of the BELs, the FWHM and σ_l of CIV and the flux level of the continuum at 1350 Å for 95 sources. From these I calculated the resulting metallicities, luminosities and SMBH masses. M. Vestergaard provided the $\frac{FeII}{MgII}$-ratio for 86 sources. Firstly the results are presented thereafter I compare them to each other in order to determine if the parameters are correlated.

The typical level of the emission line strength for an important emission line such as CIV was in the range of ∼300-500 $\cdot$ 10^{-16}erg·s^{-1}cm^{-2} with a typical error of <1%. In comparison one of the weak emission lines HeII had a line strength of around ∼37 $\cdot$ 10^{-16}erg·s^{-1}cm^{-2} with a typical error of around ∼25%. The higher error associated with the range where HeII is observed at is a result of a noisier spectrum than for the range where CIV is observed because there were often absorption and HeII blended with OIII], this effect is obviously more serious for weak lines such as these in comparison to CIV which also had absorption. The higher percentage error of the weaker lines also accentuates that the strong emission lines have more accurate measures of the emission line strength making the strong lines crucial as they provide very accurate emission line ratios. For the interested reader all the line strengths are presented in appendix B.2.

One of the main objectives are to determine the metallicity for as many sources as possible. Metallicity estimates have been created for 95 of the original 100 QSOs from the XQ-100 legacy survey. The metallicity estimates can be seen in appendix B.3. The range of the metallicity is from 0.5-10 $Z_\odot$ with a mean value at 2.79 $\pm$ 0.25 $Z_\odot$. This should be compared to the metallicity estimates determined by Dietrich et al. (2003b) who found an average metallicity of 5.3 $\pm$ 0.3 $Z_\odot$ for their sample of 70 QSOs, which was at the same redshift as my sample of QSOs. The reason for the different metallicity estimates is likely due to the fact that Dietrich et al. (2003b) and I use different methods to obtain them.

Dietrich et al. (2003b) used the segmented power law and I use the hard power law. Dietrich et al. (2003b) have compared the metallicity estimates obtained using the different continuum models and found that this could cause a difference of up to a factor of ∼2. The hard continuum model provides lower metallicity estimates than the segmented model, where the difference is especially prominent for $\frac{NV}{CIV}$ and $\frac{NV}{HeII}$ (see figure 6). These line ratios are the ones for which it have been possible to obtain the most measurements of, making them very important. Another difference in our

approach is how we have combined the metallicity estimates from the different line ratios. I used inverse variance weighting, where the variance is the uncertainty of the emission line flux based on the uncertainty of the continuum fit (see sections 3.2.2 and 3.2.5) whereas Dietrich et al. (2003b) used the average of the metallicity estimates based on the different line ratios. The inverse variance weighting scheme means that the metallicity estimates with low errors are weighted higher and those with larger errors are weighted less (e.g. the metallicity from $\frac{NV}{CIV}$ is wheighted higher than the metallicity based on the weak lines (e.g., $\frac{NIV]}{OIII]}$)). Because $\frac{NV}{CIV}$ is weighted highest and have a larger difference in the metallicity estimates i.e. lower metallicity estimates. The average weighted metallicity I obtain should provide lower metallicity estimates than those found by Dietrich et al. (2003b) as seen in figure 21.

Another point is that Dietrich et al. (2003b) could have overestimated NV, if Ly-α was severely blended with NV. This problem was not discussed in the paper but from the investigation of the spectra I know that this is a possible explanation for high metallicity measurements. This would lead to generally higher metallicity estimates than what I find. Another difference in the results is that Dietrich et al. (2003b) measures many more NIV emission lines in the spectra of his sample, than I am able to. This strikes me as odd because this specific line is very hard to measure and it is seldom present in my spectra. The reason why Dietrich et al. (2003b) have measured this many NIV emission lines may be due to a too optimistic approach or simply that many more NIV lines were present. QSOs with strong nitrogen lines have been observed (Baldwin et al. 2003), hence the QSO sample investigated by Dietrich et al. (2003b) may have contained such "Nitrogen-loud" QSOs. But if there were "Nitrogen-loud" QSOs in the sample Dietrich et al. (2003b) used there should also be "Nitrogen-loud" QSOs in the sample I used, since the QSO samples we used are very similar i.e. luminous QSOs with high redshift. It should also be noted that I calibrated the metallicity for $\frac{NIII]}{CIII]}$ and $\frac{NIV]}{OIII]}$ which lowered the metallicity estimate based on these two line ratios.

These combined contributions to a lower metallicity than the one determined by Dietrich et al. (2003b) is likely to be the cause of our different metallicity estimates. But if I look at the general trends of how the metallicity estimates from the different line ratios compare Dietrich et al. (2003b) and I have found the same scatter in the metallicities for the same comparisons of the metallicity estimates based on the different emission line ratios (see e.g. figures 20 and 21). Therefore it seems that the difference in our results is primarily in the absolute metallicity level. This is less important since my focus is on the relative variation of metallicity with other physical parameters rather than determining absolute metallicity levels.

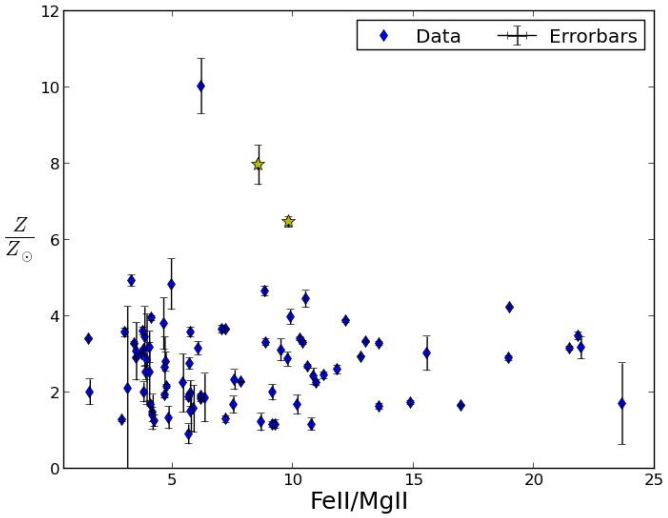

Fig. 33.— The $\frac{FeII}{MgII}$ relation with the metallicity Z. Note that one measurement have a high $\frac{FeII}{MgII}$-ratio of ~ 40 which is not shown.

The SMBH mass was also estimated for 95 QSOs with a mean of: $\log(M_{BH,comb})$ =9.42 $\pm$ 0.46 dex. The mass estimates for all the sources can be seen in appendix B.4. The SMBH masses I have measured are in general a bit higher than the masses of the Bright Quasar Survey QSOs measured by Vestergaard & Peterson (2006) but this could be due to the fact that the QSOs in the XQ-100 Legacy Survey are more luminous than those of the Bright Quasar Survey. I determined the continuum luminosities on the basis of the 1350 Å continuum emission, which can be seen alongside the SMBH mass estimates in appendix B.4.

We now have all we needed in order to investigate the presence of any relationships between the parameters just presented i.e. the combined SMBH mass, the metallicity and the $\frac{FeII}{MgII}$-ratio. Since the main focus of this thesis has been on testing the hypothesis that the $\frac{FeII}{MgII}$-ratio scale with the metallicity I present this firstly, see figure 33. From the plot it is evident that there is no relation between the $\frac{FeII}{MgII}$-ratio and the metallicity obtained from the BEL line ratios. There are a couple of outliers at high metallicity and one $\frac{FeII}{MgII}$ measurement that falls outside of the range shown in the figure. The reason for the high metallicity estimates can for two of the sources (marked with yellow stars in figure 33) be explained by the fact that their Ly-α and NV emission lines are severely blended. Hence the metallicity estimates from these cannot be trusted as previously discussed in section 3.2.5.2. The remaining outlier in

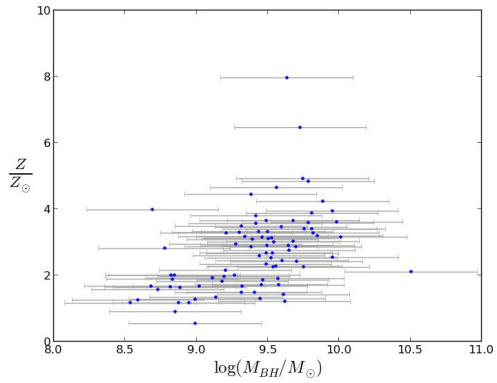

Fig. 34.— Comparison between the metallicity and the SMBH mass.

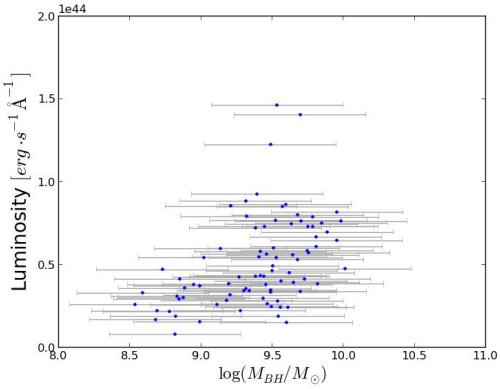

Fig. 35.— Comparison between the SMBH mass and the Luminosity.

metallicity cannot be explained and may be an especially metal rich source. The cause of the extreme outlier, for which $\frac{FeII}{MgII} = 40$, is a non-optimal fit of the FeII pseudo-continuum (private communications M. Vestergaard, 2015). The outliers do not affect the general trend of the data and it is pretty clear that there is no relation between $\frac{FeII}{MgII}$ and the metallicity. I also investigated if the $\frac{FeII}{MgII}$-ratio scaled with the redshift and the mass but it did not, the plots are shown in appendix F and G.

The next step in my analysis was to compare the mass with the luminosity, the redshift and the metallicity. This is presented in figure 34, 35 and 37. Here it can be seen that there is no relation with the redshift but both the mass-luminosity and mass metallicity seems to have higher values for objects with higher black hole masses. The relations are not strong but show a general trend that for higher SMBH masses the luminosity and metallicity is higher. This is very interesting because it supports that QSOs have similar relations as galaxies i.e. mainly a mass-metallicity relation and a mass-luminosity relation. Another parameter that is helpful to introduce is; $\frac{L_{bol}}{L_{edd}}$, as this is an indicator of the activity of QSOs. Here L_{bol} is the bolometric luminosity which is determined on the basis of the continuum at 2100 Å and L_{edd} is the Eddington luminosity which can be thought of as the highest possible luminosity of an object of mass M powered by spherical accretion (Peterson 1997). L_{bol} can be expressed as: $L_{2100} \cdot 2100 \cdot BC$, where BC is the scaling factor from the continuum level at one point to the bolometric luminosity (Richards et al. 2006). The reason $\frac{L_{bol}}{L_{edd}}$ is an indicator of the activity of QSOs is because it equals $\frac{\dot{M}}{\dot{M_{edd}}}$ where, $\dot{M}$, is the mass-accretion rate of the SMBH and $\dot{M_{edd}}$ is the Eddington mass-accretion rate (Peterson 1997). The equation showing the relation between L and $\dot{M}$ was presented in section 2.1.1. Hence $\frac{L_{bol}}{L_{edd}}$ is related to the mass-accretion rate which is a measure of the activity of QSOs.

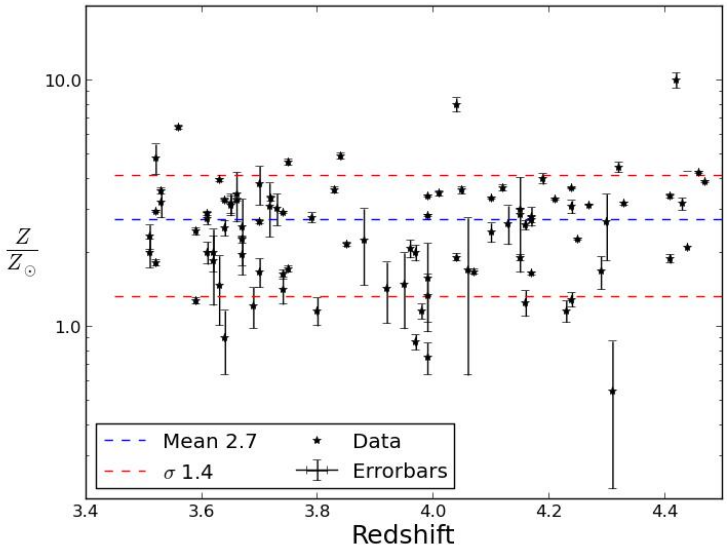

Fig. 36.— Comparison between the redshift and average metallicity estimate from the BEL line ratios.

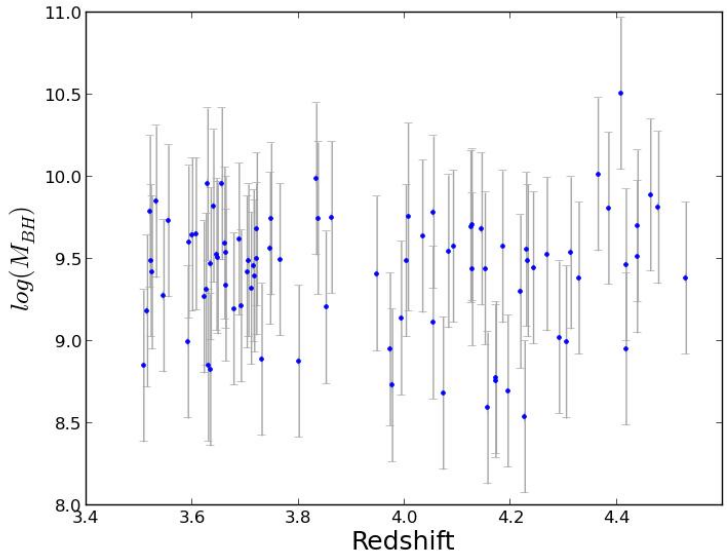

Fig. 37.— Comparison between the redshift and the SMBH mass.

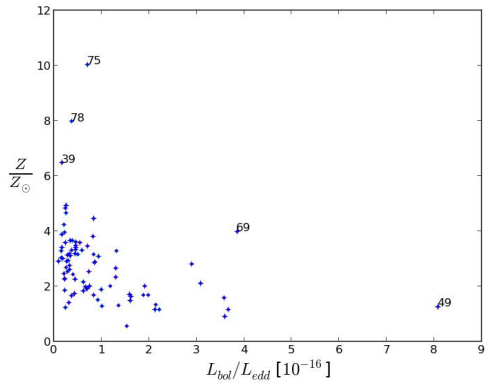

Fig. 38.— Comparison between the metallicity and the $\frac{L_{bol}}{L_{edd}}$. The outliers have been annotated with their according SDSS numbers.

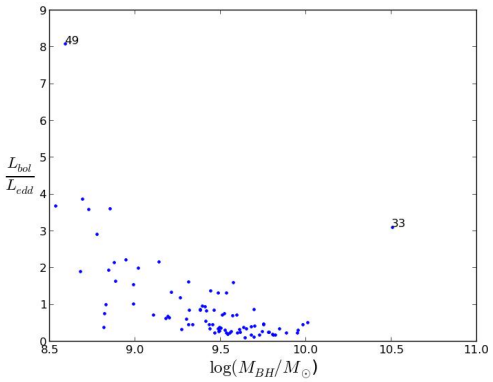

Fig. 39.— Comparison between the SMBH mass and the $\frac{L_{bol}}{L_{edd}}$. The outliers have been annotated with their according SDSS numbers.

It is believed that QSOs were most active when they were young whereafter the activity decreased as the QSOs get older. It would be interesting if this could be seen in the data. Hence it is obvious to compare $\frac{L_{bol}}{L_{edd}}$ to the metallicity because as previously mentioned a younger system should have a lower degree of chemical enrichment than an old QSO. The comparison of the $\frac{L_{bol}}{L_{edd}}$ with the metallicity is presented in figure 38. From this it can be seen that the majority of the sources are at low $\frac{L_{bol}}{L_{edd}}$ i.e. they have low activity and therefore thought to be old and a few of the sources have higher $\frac{L_{bol}}{L_{edd}}$. A general trend can be seen where QSOs with low $\frac{L_{bol}}{L_{edd}}$ have higher metallicities than the high $\frac{L_{bol}}{L_{edd}}$. This supports the idea that young sources have low metallicities and old sources have high metallicities. I have investigated the outliers in order to make sure that these estimates were sound and found that source #9 had a non-optimal fit of NV which would lead to a higher uncertainty in the metallicity than what is presented in the plot. I again note that source #39 and #78 have severely blended Ly-α-NV complex which makes the metallicity determination unreliable. But even removing these points does not eliminate the relation. I then compared $\frac{L_{bol}}{L_{edd}}$ with the redshift and the SMBH mass. I found no relation between the $\frac{L_{bol}}{L_{edd}}$ and the redshift, see appendix H, but there was a relation between $\frac{L_{bol}}{L_{edd}}$ and the SMBH mass, see figure 39. It seems obvious that there should be a relation between the two since L_{edd} is proportional to the mass so this is mostly a sanity check. I have now compared the luminosity, metallicity, redshift, $\frac{FeII}{MgII}$-ratio and $\frac{L_{bol}}{L_{edd}}$. The general picture is that the luminosity, metallicity, mass-accretion rate and mass does not show a relation with the redshift and the $\frac{FeII}{MgII}$-ratio. This is interesting because some dependency on especially the redshift would be expected, but this will be discussed in the next section.

5. Discussion

In this section I discuss the main results which are that no relation between the $\frac{FeII}{MgII}$-ratio and the metallicity have been found. I also discuss the secondary results; That the mass, metallicity and $\frac{L_{bol}}{L_{edd}}$-ratio exhibits relationships between these physical parameters. I also discuss the determined metallicities and how they relate to observations and our physical understanding of QSOs.

5.1. The Absent $\frac{FeII}{MgII}$ - Metallicity Relation

A possible explanation for the lack of relation between the $\frac{FeII}{MgII}$-ratio and the metallicity could be that the range of $\frac{FeII}{MgII}$-ratios is to narrow to see a relation. But since the range of $\frac{FeII}{MgII}$ is ∼1-25 it should be wide enough, in comparison the range of BEL ratios for e.g. the $\frac{NV}{CIV}$ was ∼0.5-10. Therefore another explanation for the lack of observed relation between the metallicity and the $\frac{FeII}{MgII}$-ratio must be found. A possible explanation is that the $\frac{FeII}{MgII}$-ratio is more sensitive to other parameters than the abundances, which I have previously mentioned in section 2.2.2 to be a major concern. Baldwin et al. (2004) have shown that the FeII emission is dependent on many things such as: the column density, the microturbulence, the temperature, the abundance and the ionizing photon flux of the BLR. Ferland et al. (2009) have later shown that models with infalling FeII emitting clouds are consistent with observations of the FeII emission. Therefore the current paradigm is: infalling FeII emitting gas clouds to explain the observations.

Because I have seen no relation between the $\frac{FeII}{MgII}$-ratio with the metallicity I can conclude that the FeII pseudo-continuum emission is not dominated by the abundance of Fe. This problem could be solved by using the optical FeII emission at 4000-6000 Å which have been shown to be more dependent on the abundance than the UV FeII emission (2000-3000 Å) (Baldwin et al. 2004; Verner et al. 2003). Verner et al. (2003) suggest combining $\frac{FeII(UV)}{MgII}$ with $\frac{FeII(UV)}{FeII(optical)}$ as this provides a reliable abundance measure of $\frac{Fe}{Mg}$. The reason why UV FeII is less sensitive to the abundance lie in the electron structure of FeII. The UV FeII transitions arise from high excitation levels and the density of the levels increase substantially above 10 eV. The UV transitions of FeII are closer in energy than the optical FeII transitions and their strengths are more affected by microturbulence than those of the optical lines. Therefore the UV FeII is more sensitive to microturbulence than the optical FeII emission.
Therefore it would be preferable to use the optical FeII emission to obtain the

abundance of FeII. Modelling the optical FeII emission can be accomplished by using templates of the optical FeII emission, in the same manner as described in section 3.2.6 (Vestergaard & Wilkes 2001; Véron-Cetty et al. 2004). Measurements of optical FeII would however not be possible for the spectra used in this thesis. Because the optical FeII emission lie in the near infra red where telluric absorption is strong and the telluric corrections are unreliable. It would be possible to obtain the emission line strength for optical FeII for low redshift QSOs which have been done by Shields et al. (2010). In their paper they also present another explanation for the spread in the FeII emission line strength which could be due to the depletion of FeII into grains in the low ionization part of the BLR. This would affect the FeII emission differently for each object in accordance with the degree of grain depletion and can explain the difference in the FeII emission strength (Shields et al. 2010).

The next thing to asses, regarding the use of the $\frac{FeII}{MgII}$-ratio as a metallicity tracer, is whether the QSO sample I have used is representative of the QSO population in general. The sample I used contains very bright QSOs with BELs observed at high redshift. Dietrich et al. (2003c) have shown that AGNs have very similar BELs over a wide range in luminosity and redshift. This was done by investigating 744 AGN spectra for which they modelled the BELs as well as the continuum and showed a correlation with the equivalent width of the BELs with the continuum luminosity (at 1450 Å). If QSO spectra are very similar they must have been formed in a similar environment. So there should not be a significant difference in a QSO sample of low redshift from a QSO sample of high redshift. Therefore there should not be a difference in how the $\frac{FeII}{MgII}$-ratio correlates with the metallicity from a high redshift sample to a low redshift sample of QSOs. Therefore my findings apply to all QSOs throughout the redshifted universe. Thus the $\frac{FeII}{MgII}$-ratio should be discarded as a metallicity tracer for all QSOs.

5.2. Metallicity

Since I discard using the $\frac{FeII}{MgII}$-ratio as a reliable tracer for the metallicity a better method to obtain the metallicity for QSOs is to use the emission line ratios from the BELs (see section 2.2.1). This method is better to use since it have been shown to scale with the metallicity and provides metallicity estimates from the different line ratios that are consistent to within $\sim 1\sigma$. But some of the emission line ratios are not optimal to use as metallicity estimates. This became clear to me when I compared the metallicity estimates from the different line ratios, see appendix B.1. When I compared the metallicity obtained from different Nitrogen transitions the results were scatter plots (see figures in appendix C). As I compared all the metallicity estimates

based on different emission line ratios and have observed that $\frac{NV}{HeII}$ and $\frac{NV}{CIV}$ have a strong correlation with each other, the metallicity estimates for the remaining emission line ratios should also scale with the metallicities obtained from these two line ratios. I compared my result with those of Dietrich et al. (2003b), they also found scatter plots for the same comparison of the metallicity, although they did not show all the possible combinations of comparisons between the metallicity estimates from the different line ratios. Hence it appears that the lack of correlation, when comparing metallicity estimates from different Nitrogen transitions, is either due to constraints in the precision of the measurements of the emission line ratios, e.g. measurements of severely blended Ly-α and NV or due to the physics of the emission line ratios i.e. the line ratios sensitivity of e.g. temperature.

Uncertainties in the measurements are especially prominent for the weak Nitrogen line, NIV, which may be associated with too high errors to obtain accurate metallicity estimates. This may be due to the fact that some of the line ratios are affected by other parameters than the abundance, such as the temperature of the BLR gas, which is the case for e.g. $\frac{NIII]}{CIII]}$. The line ratios which have provided the strongest 1-1 correlation are the $\frac{NV}{CIV]}$-ratio and the $\frac{NV}{HeII]}$-ratio, which are also the emission line ratios with the most observations. Severely blended NV lines should be disregarded as their line strengths are not properly constrained. Even though there are many things that should be taken into account the metallicity estimates obtained from $\frac{NV}{CIV]}$ and $\frac{NV}{HeII]}$ are consistent to within $\sim 1.4\sigma$, for metallicities lower than 4 $Z_{\odot}$. But as I did not obtain many measurements of the emission line strengths of NIV (I obtained eight emission line strengths of NIV) it may be wise to investigate this further before discarding the metallicity estimates based on NIV completely. When I compared the metallicity estimates based on different Nitrogen lines no correlation could be seen.

The metallicity level I measured was at ~ 3 $Z_{\odot}$ this should be compared to the mean metallicity of the core of massive galaxies which for low redshift galaxies are typically $\sim$2-9 $Z_{\odot}$ Hamann & Ferland (1999). Therefore my findings of the metallicity in QSOs corresponds to the metallicity in the core of galaxies which is expected. The difference in the method used to obtain the metallicity is different for galaxies and QSOs, as mentioned in section 2.2. The high chemical enrichment in the centre of spiral galaxies may come as a surprise when compared to the chemical enrichment in the solar neighbourhood. The explanation as to why it is still meaningful is that the chemical enrichment have a gradient in the metallicity i.e. the metallicity decrease as we move away from the centre. The high degree of chemical enriched gas in the centre is due to star formation because the centre is where the most gas is available. The gas needed for starformation is cool molecular gas which can be expelled if events

of violent starbursts occur. The reason for the high degree of chemical enrichment in QSOs may be answered from the formation of QSOs, which may have happened in massive starbursts. This could have created a highly chemically enriched gas around the QSO, which we would later observe in the core of galaxies.

5.3. The Mass, Metallicity, Luminosity and $\frac{L_{bol}}{L_{edd}}$ Relationships

The mass-metallicity plot presented in the previous section indicates the presence of a mass-metallicity relation namely that the metallicity increases for more massive black holes (see figure 34). The fact that we see a relation between the mass of the SMBH and the metallicity is interesting because it can tell us something about the evolution of the BLR gas and QSOs in general. Assuming that the SMBH masses are generally higher for older QSOs the mass-metallicity relation indicates co-evolution of the QSO with the host galaxy. A rise in the metallicity with higher SMBH masses means that a maturing of the BLR must have taken place where stellar processes is most likely to account for the chemical enrichment. It could be interesting to investigate if this relation can be seen for the final stage of QSOs, which is believed to be central SMBHs in large spheroidal galaxies. This has been done by Tremonti et al. (2004) who show that the metallicity and mass of the galaxies have a tight ($\pm$0.1 dex) correlation. This correlation is much tighter than the one I have found to be present between the mass of the SMBH and the metallicity of the BLR for QSOs. This may be due to the difference in the methods used to obtain the mass and the metallicity of the two systems respectively. I have used the BELs to obtain the metallicities of the BLR and Tremonti et al. (2004) have used nebular Oxygen emission lines to obtain the metallicity of galaxies. The reason this would be interesting is it may be possible to find extinguished QSOs and see how the mixing of the central gas have affects the further evolution of the galaxy. But that undertaking is beyond the scope of this thesis.

Another interesting relation I have shown (see section 4) was the mass-luminosity relation. This relation have also been shown to exist for galaxies but it is believed to be caused by different processes than those for QSOs. The mass-luminosity relation for galaxies is mainly due to more stars being created in higher mass galaxies because there should be more gas to create stars. For QSOs the mass-luminosity relation is due to a higher accretion rate since higher mass SMBHs in QSOs have higher accretion rates which leads to a higher luminosity (remember equation 1). So for galaxies the mass-luminosity is mainly caused by stellar processes and for QSOs it is due to the SMBHs accretion rate. Hence this may appear to be very different causes but for both QSOs and galaxies the higher mass is caused by a higher gravitational potential which have lead to the assembling of gas which have lead to the evolution we observe making

this self-reinforcing.

The mass-accretion rate was also compared to the mass and the metallicity, where the shown relation with the metallicity is of special interest (see figures 38 and 39). In this relation I observe that the activity is highest for low metallicity QSOs. This could be interpreted to mean that young QSOs have undergone less chemical enrichment than old QSOs which is in line with what we saw for the mass-metallicity relation. Here the $\frac{L_{bol}}{L_{edd}}$-ratio is a better measure for the actual age of the QSO than the mass. This is because the initial mass of a population of QSOs will have different SMBH masses rather than just one specific mass for all SMBHs in QSOs. The $\frac{L_{bol}}{L_{edd}}$-ratio will also have some spread in the relation with the metallicity but it still provides a better measure of where in the evolutional phase the QSO is in comparison to the SMBH mass. This is reflected in my observations since the mass-accretion rate to metallicity have a tighter relation than the mass-metallicity relation (see figures 34 and 38).

It is reassuring to have found relations between the mass, metallicity, luminosity and activity because this provide further evidence that the reason why the $\frac{FeII}{MgII}$-ratio have not been shown to correlate with the metallicity should be found in the fact that the $\frac{FeII}{MgII}$-ratio is a bad estimate of the $\frac{Fe}{Mg}$-ratio. Hence having shown a relation between the mass, metallicity, luminosity and activity for this QSO sample means that we should have seen a relation between the $\frac{FeII}{MgII}$-ratio and the metallicity. But the reason that no relation have been established is because the FeII pseudo-continuum emission is much more affected by other parameters than the abundance.

6. Conclusion

I have analyzed 100 luminous high redshift QSO spectra from the XQ-100 Legacy Survey for this study. I argue that the sample is representative of the QSO population based on the similarity of their BEL spectra. The QSOs in this survey does not have any special features that should falsify this assumption.

I have shown that the $\frac{FeII}{MgII}$ does not scale with the metallicity. The reason for this is most likely that the $\frac{FeII}{MgII}$-ratio does not scale with the $\frac{Fe}{Mg}$ abundance ratio because the $FeII$ emission is more sensitive to the physical condition in the BLR. Therefore another measure for the $\frac{Fe}{Mg}$ abundance ratio should be used than the $\frac{FeII}{MgII}$-ratio, if this is still desirable. A possibility of measuring the $\frac{Fe}{Mg}$ abundance ratio could be using the optical FeII emission since this is more sensitive to the abundance than the UV FeII emission is.

I also investigated certain correlations between the mass, metallicity, luminosity, mass-accretion rate and redshift. I found no redshift dependencies for any of the parameters. I have found the following relations: mass-metallicity, mass-luminosity, "mass-accretion rate"-metallicity and "mass-accretion rate"-luminosity. I discuss this and conclude that the relations present in the sample is an indicator of co-evolution between QSOs and their host galaxies.

REFERENCES

Baldwin, J. A., Ferland, G. J., Korista, K. T., Hamann, F., & LaCluyzé, A. 2004, Astrophysical Journal, 615, 610

Baldwin, J. A., Hamann, F., Korista, K. T., Ferland, G. J., Dietrich, M., & Warner, C. 2003, Astrophysical Journal, 583, 649

Bell, M. B. 2004, ArXiv Astrophysics e-prints

Bentz, M., Manne-Nicholas, E., Onken, C., & Valluri, M. 2013, A Stellar Dynamical Black Hole Mass for the Reverberation-Mapped Active Galaxy NGC6814, NOAO Proposal

Cox, A. N. 2000, Allen's astrophysical quantities

Davidson, K., & Netzer, H. 1979, Reviews of Modern Physics, 51, 715

De Rosa, G., Decarli, R., Walter, F., Fan, X., Jiang, L., Kurk, J., Pasquali, A., & Rix, H. W. 2011, Astrophysical Journal, 739, 56

De Rosa, G., Venemans, B. P., Decarli, R., Gennaro, M., Simcoe, R. A., Dietrich, M., Peterson, B. M., Walter, F., Frank, S., McMahon, R. G., Hewett, P. C., Mortlock, D. J., & Simpson, C. 2014, Astrophysical Journal, 790, 145

Decarli, R., Falomo, R., Treves, A., Labita, M., Kotilainen, J. K., & Scarpa, R. 2010, Monthly Notices of the Royal Astronomical Society, 402, 2453

Dietrich, M., Appenzeller, I., Hamann, F., Heidt, J., Jäger, K., Vestergaard, M., & Wagner, S. J. 2003a, Astronomy and Astrophysics, 398, 891

Dietrich, M., & Hamann, F. 2008, in Revista Mexicana de Astronomia y Astrofisica, vol. 27, Vol. 32, Revista Mexicana de Astronomia y Astrofisica Conference Series, 65–68

Dietrich, M., Hamann, F., Appenzeller, I., & Vestergaard, M. 2003b, The Astrophysical Journal, 596, 817

Dietrich, M., Hamann, F., Shields, J., Constantin, A., & Vestergaard, M. 2003c, in Astronomical Society of the Pacific Conference Series, Vol. 290, Active Galactic Nuclei: From Central Engine to Host Galaxy, ed. S. Collin, F. Combes, & I. Shlosman, 607

Dietrich, M., Hamann, F., Shields, J. C., Constantin, A., Heidt, J., Jäger, K., Vestergaard, M., & Wagner, S. J. 2003d, Astrophysical Journal, 589, 722

Emerson, D. 1996, Interpreting Astronomical Spectra

Ferland, G. J., Hu, C., Wang, J.-M., Baldwin, J. A., Porter, R. L., van Hoof, P. A. M., & Williams, R. J. R. 2009, The Astrophysical Journal Letters, 707, L82

Gebhardt, K., Kormendy, J., Ho, L. C., Bender, R., Bower, G., Dressler, A., Faber, S. M., Filippenko, A. V., Green, R., Grillmair, C., Lauer, T. R., Magorrian, J., Pinkney, J., Richstone, D., & Tremaine, S. 2000, The Astrophysical Journal, 543, L5

Hamann, E., & Ferland, G. 1993a, Revista Mexicana de Astronomia y Astrofisica, 26, 53

Hamann, F., & Ferland, G. 1993b, Astrophysical Journal, 418, 11

—. 1999, Annual Review of Astronomy and Astrophysics, 37, 487

Hamann, F., Korista, K. T., Ferland, G. J., Warner, C., & Baldwin, J. 2002, Astrophysical Journal, 564, 592

Hamann, F., & Simon, L. E. 2010, in IAU Symposium, Vol. 265, IAU Symposium, ed. K. Cunha, M. Spite, & B. Barbuy, 171–178

Hogg, D. W. 1999, ArXiv Astrophysics e-prints

Hopkins, P. F., Lidz, A., Hernquist, L., Coil, A. L., Myers, A. D., Cox, T. J., & Spergel, D. N. 2007, Astrophysical Journal, 662, 110

Hopkins, P. F., Somerville, R. S., Hernquist, L., Cox, T. J., Robertson, B., & Li, Y. 2006, Astrophysical Journal, 652, 864

Kaspi, S., Maoz, D., Netzer, H., Peterson, B. M., Vestergaard, M., & Jannuzi, B. T. 2005, Astrophysical Journal, 629, 61

Korista, K., Baldwin, J., Ferland, G., & Verner, D. 1997, ApJS, 108, 401

Longair, M. S. 2000, Galaxy Formation

Mathews, W. G., & Ferland, G. J. 1987, Astrophysical Journal, 323, 456

Mortlock, D. J., Warren, S. J., Venemans, B. P., Patel, M., Hewett, P. C., McMahon, R. G., Simpson, C., Theuns, T., Gonzáles-Solares, E. A., Adamson, A., Dye, S., Hambly, N. C., Hirst, P., Irwin, M. J., Kuiper, E., Lawrence, A., & Röttgering, H. J. A. 2011, Nature, 474, 616

Netzer, H., & Marziani, P. 2010, Astrophysical Journal, 724, 318

Peterson, B. M. 1997, An Introduction to Active Galactic Nuclei

—. 2011, ArXiv e-prints

Peterson, B. M., Ali, B., Horne, K., Bertram, R., Lame, N. J., Pogge, R. W., & Wagner, R. M. 1993, Astrophysical Journal, 402, 469

Richards, G. T., Lacy, M., Storrie-Lombardi, L. J., Hall, P. B., Gallagher, S. C., Hines, D. C., Fan, X., Papovich, C., Vanden Berk, D. E., Trammell, G. B., Schneider, D. P., Vestergaard, M., York, D. G., Jester, S., Anderson, S. F., Budavári, T., & Szalay, A. S. 2006, The Astrophysical Journal Supplement Series, 166, 470

Scannapieco, E., & Bildsten, L. 2005, Astrophysical Journal, 629, L85

Shen, Y., Richards, G. T., Strauss, M. A., Hall, P. B., Schneider, D. P., Snedden, S., Bizyaev, D., Brewington, H., Malanushenko, V., Malanushenko, E., Oravetz, D., Pan, K., & Simmons, A. 2011, Astrophysical Journal Supplements, 194, 45

Shields, G. A. 1976, Astrophysical Journal, 204, 330

Shields, G. A., Ludwig, R. R., & Salviander, S. 2010, Astrophysical Journal, 721, 1835

Shlosman, I., Begelman, M. C., & Frank, J. 1990, Nature, 345, 679

Sparke, L. S., & Gallagher, III, J. S. 2007, Galaxies in the Universe: An Introduction (Cambridge University Press)

Stahler, S. W., & Palla, F. 2005, The Formation of Stars

Tanvir, N. R., Fox, D. B., Levan, A. J., Berger, E., Wiersema, K., Fynbo, J. P. U., Cucchiara, A., Krühler, T., Gehrels, N., Bloom, J. S., Greiner, J., Evans, P. A., Rol, E., Olivares, F., Hjorth, J., Jakobsson, P., Farihi, J., Willingale, R., Starling, R. L. C., Cenko, S. B., Perley, D., Maund, J. R., Duke, J., Wijers, R. A. M. J., Adamson, A. J., Allan, A., Bremer, M. N., Burrows, D. N., Castro-Tirado, A. J., Cavanagh, B., de Ugarte Postigo, A., Dopita, M. A., Fatkhullin, T. A., Fruchter, A. S., Foley, R. J., Gorosabel, J., Kennea, J., Kerr, T., Klose, S., Krimm, H. A., Komarova, V. N., Kulkarni, S. R., Moskvitin, A. S., Mundell, C. G., Naylor, T., Page, K., Penprase, B. E., Perri, M., Podsiadlowski, P., Roth, K., Rutledge, R. E., Sakamoto, T., Schady, P., Schmidt, B. P., Soderberg, A. M., Sollerman, J., Stephens, A. W., Stratta, G., Ukwatta, T. N., Watson, D., Westra, E., Wold, T., & Wolf, C. 2009, Nature, 461, 1254

Tremonti, C. A., Heckman, T. M., Kauffmann, G., Brinchmann, J., Charlot, S., White, S. D. M., Seibert, M., Peng, E. W., Schlegel, D. J., Uomoto, A., Fukugita, M., & Brinkmann, J. 2004, ApJ, 613, 898

Urry, C. M., & Padovani, P. 1995, Publications of the Astronomical Society of the Pacific, 107, 803

Verner, E., Bruhweiler, F., Verner, D., Johansson, S., & Gull, T. 2003, Astrophysical Journal, 592, L59

Verner, E., Bruhweiler, F. C., & Long, T. 2011, AGU Fall Meeting Abstracts, A721

Véron-Cetty, M.-P., Joly, M., & Véron, P. 2004, Astronomy and Astrophysics, 417, 515

Vestergaard, M., Denney, K., Fan, X., Jensen, J. J., Kelly, B. C., Osmer, P. S., Peterson, B. M., & Tremonti, C. A. 2011, in Narrow-Line Seyfert 1 Galaxies and their Place in the Universe, 38

Vestergaard, M., & Osmer, P. S. 2009, Astrophysical Journal, 699, 800

Vestergaard, M., & Peterson, B. M. 2006, Astrophysical Journal, 641, 689

Vestergaard, M., & Wilkes, B. J. 2001, Astrophysical Journals, 134, 1

Wheeler, J. C., Sneden, C., & Truran, Jr., J. W. 1989, Annual review of astronomy and astrophysics, 27, 279

Zheng, W., Kriss, G. A., Telfer, R. C., Grimes, J. P., & Davidsen, A. F. 1997, Astrophysical Journal, 475, 469

---

7. Appendix

A. Tables - Objects and their chategorizaion

A.1. Source List

Table 6: The source list for the objects used from the XQ-100 Legacy Survey. Note * is the sources where the window weights have been set for them.

Number	Source Name	z(lit)	z(PCA)
1*	SDSS J101347.29+065015.6	3.79	3.808
2*	SDSS J101818.45+054822.8	3.52	3.515
3*	SDSS J102040.62+092254.2	3.64	3.640
4	SDSS J102456.61+181908.7	3.53	3.524
5	SDSS J103221.11+092748.9	3.99	3.985
6	BR 1033-0327	4.51	4.531
7	SDSS J103446.54+110214.5	4.27	4.269
8	SDSS J103732.38+070426.2	4.10	4.127
9	SDSS J103730.33+213531.3	3.63	3.626
10	SDSS J104234.01+195718.6	3.64	3.630
11	SDSS J105434.17+021551.9	3.97	3.971
12	SDSS J105705.37+191042.8	4.10	4.128
13	SDSS J105858.38+124554.9	4.33	4.341
14	SDSS J110352.73+100403.1	3.61	3.607
15	SDSS J111008.61+024458.0	4.12	4.146
16	SDSS J110855.47+120953.3	3.67	3.678
17	SDSS J111701.89+131115.4	3.62	3.622
18	SDSS J112617.40-012632.6	3.61	3.634
19	SDSS J112634.28-012436.9	3.74	3.765
20	SDSS J113536.40+084218.9	3.83	3.834
21	[HB89] 1159+120953	3.51	3.522
22	SDSS J120210.08-005425.4	3.59	3.592
23*	SDSS J124837.31+130440.9	3.72	3.721
24	SDSS J124957.23-015928.8	3.63	3.629
25	SDSS J130452.57+023924.8	3.65	3.648
26*	SDSS J131242.87+084105.1	3.74	3.731
27	2MASS J1320299-052335	3.70	3.717
28	SDSS J132346.05+140517.6	4.04	4.054
29	BR J1330-2522	3.95	3.948
30	SDSS J133254.51+005250.6	3.51	3.508

Number	Source Name	z(lit)	z(PCA)
31	SDSS J135247.98+130311.5	3.70	3.706
32	SDSS J133653.44+024338.1	3.80	3.801
33	SDSS J1401+0244	4.44	4.408
34	PKS B1418-064	3.689	3.688
35	SDSS J141608.39+181144.0	3.59	3.593
36	SDSS J144250.12+092001.5	3.53	3.532
38	SDSS J150328.88+041949.0	3.66	3.692
39	SDSS J151756.18+051103.5	3.56	3.555
40	SDSS J152436.08+212309.1	3.61	3.600
41	SDSS J154237.71+095558.8	3.99	3.986
42	SDSS J155255.03+100538.3	3.73	3.722
43	SDSS J1621-0042	3.70	3.711
44	SDSS J163319.63+141142.0	4.33	4.365
45	CGRaBS J1658-0739	3.74	3.749
46	PSS J1723+2243	4.52	4.531
47	BR 2212-1626	3.99	3.994
48	2MASSi J2239536-055219	4.56	4.556
49	BR 2248-1242	4.16	4.157
50	PSS J2344+0342	4.24	4.248
51	BR 2213-6729	4.47	4.479
52	BR J2349-3712	4.21	4.219
53	[HB89] 0000-263	4.01	4.125
54	BR J0006-6208	4.46	4.44
55	BR J0030-5129	4.17	4.173
56	PSS J0034+1639	4.29	4.292
57	SDSS J004219.74-102009.4	3.88	3.863
58	BR 0035-25(BRI J0048-2442)	4.15	4.083
59	[HB89] 0053-284	3.62	3.635
60	[HB89] 0055-269	3.66	3.661
61	PMN J0100-2708	3.52	3.546
62	BRI J0113-2803	4.30	4.314
63	PSS J0117+1552	4.24	4.243
64	PSS J0121+0347	4.13	4.125
65	SDSS J0124+0044	3.84	3.837
66	PSS J0132+1341	4.16	4.152
67	PSS J0133+0400	4.15	4.185
68	BRI J0137-4224	3.97	3.971
69	SDSS J015339.60-001104.8	4.19	4.195

Number	Source Name	z(lit)	z(PCA)
70	PSS J0211+1107	3.98	3.973
71	PMN J0214-0518	3.99	3.977
72	BR J0234-1806	4.31	4.305
73	BRI 0241-0146	4.05	4.055
74	BR 0245-0608	4.24	4.233
75	PSS J0248+1802	4.42	4.439
76	SDSS J025518.57+004847.4	4.01	4.003
77	BR J0307-4945	4.72	4.716
78	BR J0311-1722	4.04	4.034
79	BR 0401-1711	4.23	4.227
80	BR J0415-4357	4.07	4.073
81	BR 0424-2209	4.32	4.329
82	BR 0523-3345	4.41	4.385
83	BR J0529-3552	4.17	4.172
84	BR J0529-3526	4.41	4.418
85	BR J0714-6455	4.46	4.464
86*	SDSS J074711.15+273903.3	4.17	4.133
87	SDSS J075552.41+134551.1	3.67	3.663
88*	SDSS J080050.27+192058.9	3.96	3.948
89	SDSS J081855.78+095848.0	3.67	3.656
90	SDSS J083322.50+095941.2	3.75	3.716
91	SDSS J083510.92+065052.8	3.99	4.007
92	SDSS J083941.45+031817.0	4.25	4.23
93	SDSS J092041.76+072544.0	3.64	3.646
94*	SDSS J093556.91+002255.6	3.75	3.747
95*	SDSS J093714.48+082858.6	3.70	3.703
96	BRI 0952-0115	4.43	4.418
97*	SDSS J095937.11+131215.4	4.06	4.092
98	SDSS J105340.75+010335.6	3.65	3.663
99	BRI 1108-0747	3.92	3.922
100*	SDSS J133150.69+101529.4	3.85	3.852

A.2. Grouping

Table 7: Group I to V.

Group	I	II	III	IV	V
Observed Lines	All lines	NV & CIV	NV, CIV HeII & OIII]	NV, NIV CIV, HeII OIII]	NV, CIV HeII, OIII] NIII] & CIII]
SDSS #	9, 47, 49 55, 56, 64 71, 79	3, 5, 7 12, 15, 19 24, 31, 38 40, 44, 50 51, 52, 58 61, 74, 82 84, 85, 86 91, 92	2, 4, 8 11, 14, 20 21, 22, 23 26, 28, 33 35, 37, 39 41, 43, 59 60, 62, 63 65, 66, 69 70, 72, 73 75, 76, 78 80, 81, 83 90, 93, 94 95, 96, 97 100	1, 6 53, 57	10, 16, 17 18, 25, 27 29, 30, 32 34, 36, 42 45, 67, 68 87, 88, 89 98, 99
# of sources	8	23	40	4	20

NOTE: This table shows the sources in the five different groups where the numbering follows the convention of the XQ-100 Legacy survey[11].

A.3. non-optimal fits, Blended Lines

Table 8: This table contains the SDSS object numbers for the sources which either had non-optimal modelfits or a blended Ly-α-NV complex.

	Blended lines	Non-optimal modelling
Group I	56 55,64	9,47,49
Group II		40,86
Group III		23,26,33 41,43,59 60,63,72 93,97,100
Group IV	53,57	
Group V	10,25,30 34,36,42 45,87,88 89 & 98	10,16,27 29,32,34 42 & 67

B. Tables - Measurements

B.1. Line Ratios

Table 9: The average emission line ratios for all the objects.

BEL	Emission Line Ratio
NIII]/CIII]	0.4991 ± 0.3481
NIII]/OIII]	1.9436 ± 0.4010
NIV/CIV	0.3458 ± 0.0857
NIV/OIII]	1.8409 ± 0.7290
NV/CIV]	2.8233 ± 0.1308
NV/HeII]	19.5614 ± 0.5486

B.2. Line Strength

Table 10: The Line strengths in units of 10^{-16}erg·s^{-1}cm^{-2} of the individual BELs for Group I.

BEL \ Nr	9	47	49	55
NV	620.93 ± 14.50	175.01 ± 9.20	30.60 ± 4.87	176.07 ± 1.61
NIV]	23.02 ± 14.73	47.28 ± 9.61	52.69 ± 5.20	7.74 ± 1.65
CIV	946.41 ± 14.50	627.39 ± 9.20	583.38 ± 4.87	135.02 ± 1.61
HeII	86.63 ± 14.73	67.84 ± 9.61	53.16 ± 5.20	7.68 ± 1.65
OIII]	36.13 ± 14.73	36.79 ± 9.61	35.69 ± 5.20	5.16 ± 1.65
NIII]	53.93 ± 7.14	19.27 ± 4.65	60.21 ± 2.52	21.80 ± 0.80
CIII]	224.12 ± 58.11	58.27 ± 24.14	130.80 ± 12.08	23.36 ± 3.81
BEL \ Nr	56	64	71	79
NV	305.32 ± 4.69	124.21 ± 4.31	107.08 ± 9.21	96.02 ± 1.39
NIV]	23.12 ± 4.88	29.92 ± 4.39	13.73 ± 9.40	11.70 ± 1.41
CIV	285.80 ± 4.69	124.94 ± 4.31	198.10 ± 9.21	312.66 ± 1.39
HeII	33.45 ± 2.03	23.53 ± 4.39	19.65 ± 9.40	26.83 ± 0.83
OIII]	26.28 ± 10.13	6.12 ± 4.39	15.85 ± 9.40	18.68 ± 1.41
NIII]	8.33 ± 2.36	36.54 ± 2.12	21.54 ± 4.55	5.67 ± 0.68
CIII]	49.11 ± 10.64	22.75 ± 10.33	43.91 ± 23.60	34.79 ± 3.18

Table 11: The Line strengths in units of 10^{-16}erg·s^{-1}cm^{-2} of the individual BELs for Group II.

Nr	NV	CIV
3	317.65 ± 7.99	170.66 ± 7.99
5	222.70 ± 3.87	167.29 ± 3.87
7	308.89 ± 3.28	184.90 ± 3.28
12	363.71 ± 5.25	189.40 ± 5.25
15	659.57 ± 24.58	273.70 ± 24.58
19	216.53 ± 3.43	152.26 ± 3.43
24	1269.29 ± 24.89	443.02 ± 24.89
31	337.97 ± 11.75	286.43 ± 11.75
38	721.10 ± 12.48	386.96 ± 12.48
40	453.61 ± 15.25	322.39 ± 15.25
44	283.90 ± 6.59	166.05 ± 6.59
50	133.33 ± 13.03	83.11 ± 13.03
51	380.61 ± 4.75	138.64 ± 4.75
52	107.64 ± 2.26	57.16 ± 2.26
58	128.77 ± 0.88	83.99 ± 0.88
61	245.32 ± 2.08	168.48 ± 2.08
74	341.09 ± 3.11	144.20 ± 3.11
82	313.99 ± 7.10	156.13 ± 7.10
84	12.46 ± 0.27	30.98 ± 0.27
85	457.10 ± 4.43	135.77 ± 4.43
86	236.72 ± 11.44	193.69 ± 11.44
91	376.53 ± 5.49	186.47 ± 5.49
92	170.81 ± 2.03	213.24 ± 2.03

Table 12: The Line strengths in units of 10^{-16}erg·s^{-1}cm^{-2} of the individual BELs for Group III.

Nr	NV	CIV	HeII]	OIII]
2	191.92 ± 2.52	420.54 ± 2.52	36.80 ± 2.60	20.16 ± 2.60
4	737.52 ± 8.59	371.08 ± 8.59	59.86 ± 8.76	10.45 ± 8.76
8	243.18 ± 8.74	299.17 ± 8.74	29.84 ± 8.99	14.01 ± 8.99
11	19.30 ± 0.96	167.94 ± 0.96	19.75 ± 1.01	19.70 ± 1.01
14	249.17 ± 5.17	225.07 ± 5.17	26.78 ± 5.52	23.17 ± 5.52
20	622.96 ± 6.94	300.54 ± 6.94	50.43 ± 7.25	19.42 ± 7.25
21	741.58 ± 31.48	1117.48 ± 31.48	90.37 ± 32.68	147.58 ± 32.68
22	81.70 ± 1.48	397.59 ± 1.48	32.07 ± 1.50	20.67 ± 1.50
23	419.02 ± 4.01	379.29 ± 4.01	31.60 ± 4.11	8.58 ± 4.11
26	89.92 ± 2.35	209.27 ± 2.35	25.95 ± 2.41	22.29 ± 2.41
28	127.32 ± 1.96	214.07 ± 1.96	25.66 ± 1.98	2.95 ± 1.98
33	9639.86 ± 4768.89	12318.33 ± 4768.89	1692.65 ± 4967.25	387.24 ± 4967.25
35	237.24 ± 3.46	281.69 ± 3.46	28.94 ± 3.52	15.28 ± 3.52
37	592.20 ± 25.48	333.51 ± 25.48	27.28 ± 25.67	11.61 ± 25.67
39	688.81 ± 3.93	251.93 ± 3.93	22.34 ± 4.05	14.43 ± 4.05
41	33.79 ± 3.32	362.86 ± 3.32	48.66 ± 3.37	22.19 ± 3.37
43	317.81 ± 20.41	884.51 ± 20.41	68.46 ± 20.55	48.34 20.55
59	64.90 ± 7.41	252.00 ± 7.41	8.63 ± 7.61	7.70 ± 7.61
60	876.46 ± 71.47	591.47 ± 71.47	67.53 ± 74.49	31.72 ± 74.49
62	554.99 ± 66.88	534.65 ± 66.88	61.67 ± 68.24	31.54 ± 68.24
63	110.04 ± 4.75	482.31 ± 4.75	45.12 ± 4.93	31.03 ± 4.93
65	729.92 ± 6.94	361.82 ± 6.94	33.77 ± 7.17	17.79 ± 7.17
66	127.85 ± 2.19	130.41 ± 2.19	14.58 ± 2.32	14.15 ± 2.32
69	148.15 ± 2.15	128.59 ± 2.15	8.39 ± 2.26	7.59 ± 2.26
70	68.04 ± 3.17	372.32 ± 3.17	35.43 ± 3.25	26.79 ± 3.25
72	7.88 ± 2.45	200.17 ± 2.45	19.18 ± 2.60	2.61 ± 2.60
73	527.03 ± 6.89	232.60 ± 6.89	46.63 ± 7.48	16.97 ± 7.48
75	330.19 ± 5.41	359.82 ± 5.41	5.35 ± 5.49	30.31 ± 5.49
76	272.21 ± 2.62	190.33 ± 2.62	20.46 ± 2.69	13.40 ± 2.69
78	627.84 ± 10.41	165.30 ± 10.41	15.95 ± 11.72	5.51 ± 11.72
80	68.62 ± 1.19	135.78 ± 1.19	21.70 ± 1.24	10.04 ± 1.24
81	406.22 ± 6.24	262.43 ± 6.24	20.70 ± 6.30	12.94 ± 6.30
83	76.64 ± 1.31	156.03 ± 1.31	13.45 ± 1.33	13.82 ± 1.33
90	105.52 ± 1.85	219.88 ± 1.85	27.30 ± 1.88	15.81 ± 1.88
93	508.12 ± 14.72	557.69 ± 14.72	59.72 ± 15.19	22.53 ± 15.19
94	423.83 ± 3.64	212.56 ± 3.64	21.43 ± 3.85	22.44 ± 3.85

Nr	NV	CIV	HeII]	OIII]
95	304.54 ± 14.10	367.37 ± 14.10	17.27 ± 16.53	16.81 ± 16.53
96	238.75 ± 4.93	196.39 ± 4.93	20.20 ± 5.09	22.49 ± 5.09
97	711.94 ±266.88	1419.36 ± 266.88	204.79 ± 285.91	102.33 ± 285.91
100	235.42 ± 1.93	339.16 ± 1.93	35.03 ± 1.99	21.00 ± 1.99

Table 13: The Line strengths in units of 10^{-16}erg·s^{-1}cm^{-2} of the individual BELs for Group IV.

Nr	NV	NIV	CIV	HeII]	OIII]
1	201.15 ± 2.51	26.59 ± 2.58	191.83 ± 2.51	19.87 ± 2.58	15.41 ± 2.58
6	293.60 ± 3.44	18.61 ± 3.49	197.28 ± 3.44	20.44 ± 3.49	23.06 ± 3.49
53	393.24 ± 18.68	43.65 ± 19.30	558.79 ± 18.68	47.12 ± 19.30	8.53 ± 19.30
57	401.38 ± 11.11	13.10 ± 11.42	352.34 ± 11.11	46.86 ± 11.42	13.04 ± 11.42

Table 14: The Line strengths in units of 10^{-16}erg·s^{-1}cm^{-2} of the individual BELs for Group V.

Nr	NV	CIV	HeII]	OIII]	NIII]	CIII]
10	54.04 ± 5.96	449.12 ± 5.96	44.43 ± 6.07	22.78 ± 6.07	13.96 ± 2.94	90.82 ± 23.90
16	519.60 ± 17.25	415.49 ± 17.25	70.66 ± 17.92	40.62 ± 17.92	73.44 ± 8.68	164.67 ± 69.80
17	236.15 ± 7.87	228.25 ± 7.87	26.89 ± 7.98	22.71 ± 7.98	35.31 ± 3.87	69.63 ± 31.60
18	267.31 ± 3.10	223.76 ± 3.10	22.37 ± 3.14	14.55 ± 3.14	8.33 ± 1.52	64.35 ± 12.48
25	333.20 ± 5.68	170.67 ± 5.68	19.67 ± 6.18	15.51 ± 6.18	73.44 ± 2.99	90.55 ± 24.25
27	849.18 ± 27.28	434.68 ± 27.28	38.83 ± 31.29	35.85 ± 31.29	48.24 ± 15.16	146.29 ± 120.10
29	267.90 ± 12.36	301.01 ± 12.36	52.67 ± 13.33	23.85 ± 13.33	13.22 ± 6.46	84.37 ± 34.09
30	520.30 ± 5.57	478.08 ± 5.57	41.49 ± 5.87	18.35 ± 5.87	11.81 ± 2.84	128.32 ± 24.02
32	128.22 ± 3.85	475.52 ± 3.85	50.52 ± 3.95	21.39 ± 3.95	16.99 ± 1.91	91.36 ± 14.78
34	37.98 ± 6.97	336.43 ± 6.97	52.20 ± 7.17	38.19 ± 7.17	73.44 ± 3.47	97.91 ± 27.77
36	893.57 ± 12.96	374.63 ± 12.96	41.18 ± 13.16	19.59 ± 13.16	44.55 ± 6.37	173.03 ± 53.54
42	480.94 ± 7.00	281.69 ± 7.00	24.67 ± 7.25	15.94 ± 7.25	27.39 ± 3.51	40.27 ± 27.74
45	22.23 ± 2.74	112.62 ± 2.74	14.36 ± 3.02	16.46 ± 3.02	52.84 ± 1.46	87.56 ± 11.52
67	328.62 ± 1.62	396.63 ± 1.62	33.67 ± 1.75	24.10 ± 1.75	30.23 ± 0.85	116.84 ± 4.10
68	190.54 ± 1.64	182.79 ± 1.64	15.80 ± 1.66	10.79 ± 1.66	5.99 ± 0.80	32.80 ± 4.21
87	241.69 ± 1.78	264.51 ± 1.78	29.92 ± 1.81	16.27 ± 1.81	84.73 ± 0.88	102.82 ± 7.07
88	417.84 ± 4.22	351.76 ± 4.22	39.80 ± 4.35	16.82 ± 4.35	23.93 ± 2.11	93.76 ± 15.47
89	712.69 ± 30.13	542.47 ± 30.13	59.26 ± 30.92	24.65 ± 30.92	109.61 ± 14.98	182.06 ± 120.47
98	178.34 ± 3.47	119.25 ± 3.47	12.86 ± 3.51	15.33 ± 3.51	48.76 ± 1.70	30.01 ± 13.79
99	241.50 ± 10.57	284.72 ± 10.57	43.51 ± 11.29	49.85 ± 11.29	13.06 ± 5.47	102.72 ± 40.65

B.3. Metallicity Estimates

SDSS Number	Metallicity ± uncertainty [$Z_\odot$]
1	2.7738155 ± 0.126836
2	1.8136662 ± 0.051858
3	3.2771898 ± 0.053202
4	3.5643692 ± 0.105487
5	2.8207034 ± 0.028939
6	2.8631414 ± 0.175884
7	3.1227019 ± 0.020712
8	2.4155354 ± 0.217119
9	1.4771268 ± 0.462768
10	0.90266548 ± 0.261049
11	0.86834463 ± 0.061891
12	3.3212541 ± 0.031267
14	2.7462276 ± 0.148238
15	3.6532513 ± 0.097256
16	1.9644305 ± 0.342948
17	2.0064193 ± 0.333702
18	2.0001565 ± 0.207133
19	2.9060094 ± 0.027548
20	3.6017759 ± 0.103622
21	2.3281754 ± 0.259992
22	1.2741358 ± 0.037966
23	3.3117001 ± 0.092864
24	3.9394069 ± 0.059508
25	3.1102914 ± 0.289287
26	1.6326526 ± 0.071286
27	3.0743950 ± 0.756446
28	1.9148119 ± 0.057236
29	1.4880411 ± 0.506026
30	2.0013063 ± 0.261553
31	2.6758371 ± 0.053786
32	1.1607885 ± 0.153097
33	2.0994004 ± 2.150714
34	1.2151533 ± 0.227484
35	2.4397280 ± 0.087839
36	3.1856943 ± 0.415863
37	4.8345006 ± 0.668913

SDSS Number	Metallicity ± uncertainty [$Z_\odot$]
38	3.2771898 ± 0.036626
39	6.4644032 ± 0.128849
40	2.8911196 ± 0.058056
41	0.7514208 ± 0.110121
42	3.0192337 ± 0.447873
43	1.6699522 ± 0.222395
44	3.1549498 ± 0.046014
45	1.4113329 ± 0.178992
47	1.3373268 ± 0.298350
49	1.2514522 ± 0.149746
50	3.0654840 ± 0.184740
51	3.8687488 ± 0.036535
52	3.2940680 ± 0.044911
53	2.8545025 ± 1.191692
55	2.8046652 ± 0.248857
56	1.6751215 ± 0.254664
57	2.2433529 ± 0.766764
58	3.0062243 ± 0.012524
59	1.8552463 ± 0.633810
60	3.4518383 ± 0.788851
61	2.9360196 ± 0.015033
62	2.6568147 ± 0.796518
63	1.2917509 ± 0.088859
64	2.6255998 ± 0.469587
65	4.9223223 ± 0.151109
66	2.5894812 ± 0.114750
67	1.9028468 ± 0.052306
68	1.9990373 ± 0.148278
69	3.9777322 ± 0.191410
70	1.1566088 ± 0.080161
71	1.5691909 ± 0.614877
72	0.5465115 ± 0.326387
73	3.5767182 ± 0.116109
74	3.6467472 ± 0.023436
75	10.032076 ± 0.724884
76	3.4763279 ± 0.094202
78	7.9625458 ± 0.521618
79	1.1582176 ± 0.116724

SDSS Number	Metallicity ± uncertainty $[Z_\odot]$
80	1.6720251 ± 0.044481
81	4.4467101 ± 0.216661
82	3.3902050 ± 0.050825
83	1.8840965 ± 0.072489
84	1.6459370 ± 0.023918
85	4.2266737 ± 0.034072
86	2.7156094 ± 0.076361
87	2.2587980 ± 0.072904
88	2.0783359 ± 0.174713
89	2.5338779 ± 0.762874
90	1.7185442 ± 0.052300
91	3.3971784 ± 0.032878
92	2.2682676 ± 0.015296
93	2.5195705 ± 0.183185
94	4.6468743 ± 0.128112
95	3.7980314 ± 0.679187
96	3.1557090 ± 0.180442
97	1.7001326 ± 1.064304
98	3.1672627 ± 0.292758
99	1.4296701 ± 0.397331
100	2.1538466 ± 0.041353

B.4. Mass and Luminosity Measurements

SDSS #	$\log(M_{BH}/M_{\odot})$ (CIV, MgII)	$\log[\lambda L_{\lambda}(1350)/erg \cdot s^{-1}]$
1*	8.7273 ± 0.4624	43.4627 ± 2.7056
2	9.182 ± 0.4626	43.4521 ± 2.663
3	9.821 ± 0.4645	43.585 ± 2.4102
4	9.4167 ± 0.4669	43.6372 ± 2.4103
5*	9.4439 ± 0.4624	43.7551 ± 2.3799
6	9.3842 ± 0.4626	43.8575 ± 2.5445
7	9.5275 ± 0.4672	43.7334 ± 2.6028
8	9.7034 ± 0.4626	43.8819 ± 2.4987
9	9.3148 ± 0.4625	43.9466 ± 2.342
10	8.8529 ± 0.4626	43.6151 ± 2.5184
11*	8.4108 ± 0.4626	43.2014 ± 2.6812
12	9.4364 ± 0.4647	43.4737 ± 2.474
14	9.6517 ± 0.4626	43.5943 ± 2.5731
15	9.6813 ± 0.4639	43.9024 ± 2.3709
16	9.1939 ± 0.4625	43.5822 ± 2.5827
17	9.2664 ± 0.4627	43.6267 ± 2.5293
18	8.8233 ± 0.4627	43.2756 ± 2.644
19	9.4944 ± 0.4628	43.3915 ± 2.6228
20	9.985 ± 0.4626	43.8812 ± 2.4711
21	9.4884 ± 0.4625	44.088 ± 2.2291
22	8.9919 ± 0.4635	43.1897 ± 2.7199
23	9.4978 ± 0.4627	43.6646 ± 2.5765
24	9.9533 ± 0.4627	43.8094 ± 2.3182
25	9.5048 ± 0.4626	43.6917 ± 2.5463
26	8.8852 ± 0.4626	43.5521 ± 2.6072
27	9.3956 ± 0.4625	43.967 ± 2.2929
28	9.1105 ± 0.465	43.4091 ± 2.6754
29	9.4093 ± 0.4711	43.7368 ± 2.5761
30	8.848 ± 0.4625	43.4651 ± 2.8565
31	9.4903 ± 0.464	43.5377 ± 2.1843
32	8.8773 ± 0.4627	43.4776 ± 2.6365
33	10.5063 ± 0.4624	45.4565 ± 0.9275
34	9.6186 ± 0.4627	43.6533 ± 2.5522
35	9.6024 ± 0.4636	43.1794 ± 2.6633
36	9.8471 ± 0.4627	43.8751 ± 2.3478

SDSS #	$\log(M_{BH}/M_{\odot})$ (CIV, MgII)	$\log[\lambda L_{\lambda}(1350)/erg \cdot s^{-1}]$
37	9.7854 ± 0.4631	43.8955 ± 2.3267
38	9.2119 ± 0.4625	43.9306 ± 2.2991
39	9.7293 ± 0.4626	43.6162 ± 2.584
40	9.6463 ± 0.4656	43.7457 ± 2.4052
41*	8.5551 ± 0.4624	43.5424 ± 2.6211
42	9.6799 ± 0.4652	43.725 ± 2.5442
43	9.3198 ± 0.463	43.8977 ± 2.3463
44	10.0139 ± 0.4658	43.6756 ± 2.6158
45	9.6111 ± 0.4627	43.3843 ± 2.6741
47	9.1392 ± 0.4684	43.776 ± 2.4878
49	8.5912 ± 0.4625	43.5164 ± 2.6457
51	9.8118 ± 0.4631	43.7848 ± 2.5413
50*	9.0603 ± 0.4624	43.6615 ± 2.7458
52	9.3007 ± 0.4671	43.5333 ± 2.6116
53	9.6967 ± 0.4625	44.1479 ± 2.4478
54	9.6987 ± 0.4629	43.5294 ± 2.5636
55	8.7775 ± 0.4629	43.3363 ± 2.6736
56	9.0219 ± 0.4626	43.7349 ± 2.4904
57	9.7525 ± 0.4624	43.8639 ± 2.4972
58	9.5444 ± 0.4651	43.2765 ± 2.7217
59	9.4681 ± 0.4627	43.4182 ± 2.6097
60	9.5956 ± 0.4627	43.9366 ± 2.3272
61	9.2751 ± 0.4639	43.3468 ± 2.707
62	9.5347 ± 0.4625	44.1652 ± 2.0722
63	9.4453 ± 0.4625	43.8638 ± 2.5431
64*	7.7833 ± 0.4624	43.5600 ± 2.5913
65	9.7468 ± 0.4626	43.7666 ± 2.4369
66	9.4403 ± 0.4632	43.6316 ± 2.5659
67	9.5728 ± 0.4626	43.9292 ± 2.5088
68*	8.5143 ± 0.4625	43.3327 ± 2.6421
69	8.6943 ± 0.4629	43.342 ± 2.5419
70	8.9484 ± 0.4642	43.5779 ± 2.4631
71	8.729 ± 0.4645	43.6713 ± 2.5579
72	8.9925 ± 0.4642	43.5687 ± 2.6314

SDSS #	$\log(M_{BH}/M_{\odot})$ (CIV, MgII)	$\log[\lambda L_{\lambda}(1350)/erg \cdot s^{-1}]$
73	9.7842 ± 0.4629	43.864 ± 2.4174
74	9.4898 ± 0.4632	43.5226 ± 2.6457
75	9.5105 ± 0.4627	43.7773 ± 2.3652
76	9.3142 ± 0.4637	43.5495 ± 2.6004
78	9.6374 ± 0.465	43.872 ± 2.3927
79	8.5382 ± 0.4626	43.414 ± 2.7162
80	8.6808 ± 0.4647	43.2265 ± 2.6851
81	9.3823 ± 0.4629	43.6326 ± 2.484
82	9.8076 ± 0.4626	43.8239 ± 2.5173
83	8.83 ± 0.4642	43.4909 ± 2.5929
84	8.8196 ± 0.463	42.9029 ± 2.9969
85	9.8876 ± 0.4633	43.8416 ± 2.5272
86*	9.9415 ± 0.4624	43.7478 ± 2.3472
87	9.5367 ± 0.4629	43.4481 ± 2.6596
88*	8.6437 ± 0.4624	43.5764 ± 2.7248
89	9.9562 ± 0.4628	43.9122 ± 2.2399
90	9.4567 ± 0.4627	43.5781 ± 2.5723
91	9.7544 ± 0.5717	43.7568 ± 2.4318
92	9.5559 ± 0.4684	43.3844 ± 2.6245
93	9.5242 ± 0.4625	43.8855 ± 2.3062
94	9.5638 ± 0.4632	43.6027 ± 2.4445
95	9.4192 ± 0.4626	43.7629 ± 2.1907
96	9.4625 ± 0.4626	43.7515 ± 2.4984
97	9.5757 ± 0.4631	44.5087 ± 1.9367
98	9.3394 ± 0.4633	43.5343 ± 2.603
99*	8.6921 ± 0.4624	43.7430 ± 2.5755
100	9.2032 ± 0.4639	43.4978 ± 2.6635

C. Line Ratio Comparison with Scatter

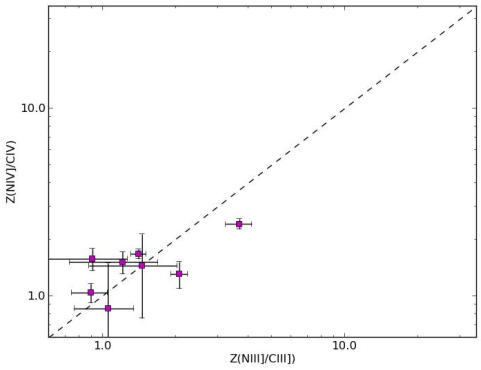

Fig. 40.— The comparison of the metallicities obtained from $\frac{NIII]}{CIII]}$ and $\frac{NIV]}{CIV}$. The dashed line is a representation of a 1-1 correlation.

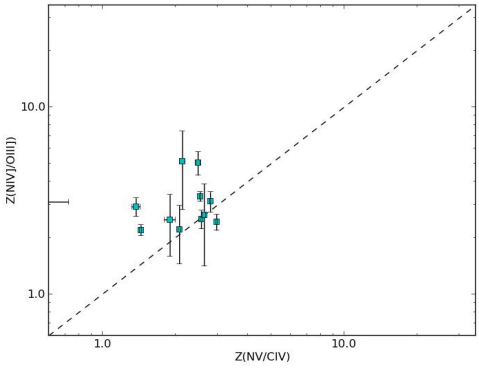

Fig. 41.— The comparison of the metallicities obtained from $\frac{NV}{CIV}$ and $\frac{NIV]}{OIII]}$. The dashed line is a representation of a 1-1 correlation.

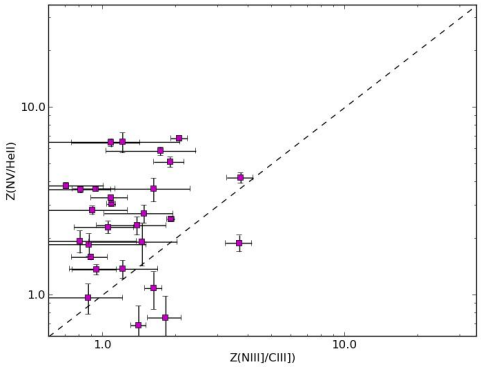

Fig. 42.— The comparison of the metallicities obtained from $\frac{NIII]}{CIII]}$ and $\frac{NV}{HeII}$. The dashed line is a representation of a 1-1 correlation.

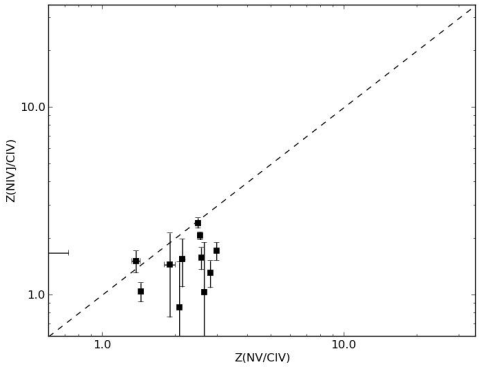

Fig. 43.— The comparison of the metallicities obtained from $\frac{NV}{CIV}$ and $\frac{NIV}{CIV}$. The dashed line is a representation of a 1-1 correlation.

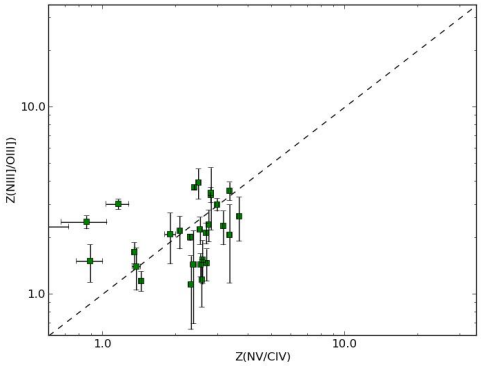

Fig. 44.— The comparison of the metallicities obtained from $\frac{NV}{CIV}$ and $\frac{NIII]}{OIII]}$. The dashed line is a representation of a 1-1 correlation.

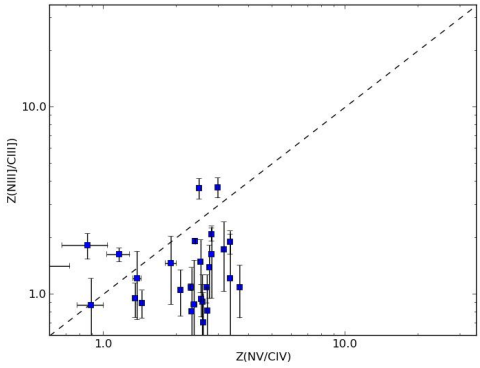

Fig. 45.— The comparison of the metallicities obtained from $\frac{NV}{CIV}$ and $\frac{NIII]}{CIII]}$. The dashed line is a representation of a 1-1 correlation.

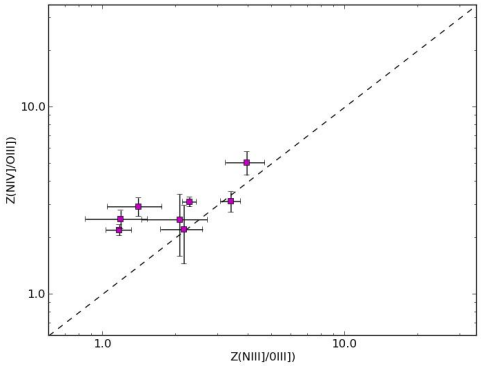

Fig. 46.— The comparison of the metallicities obtained from $\frac{NIII]}{OIII]}$ and $\frac{NIV}{OIII]}$. The dashed line is a representation of a 1-1 correlation.

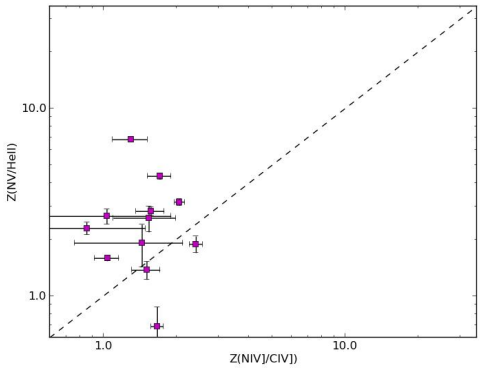

Fig. 47.— The comparison of the metallicities obtained from $\frac{NIV]}{CIV}$ and $\frac{NV}{HeII}$. The dashed line is a representation of a 1-1 correlation.

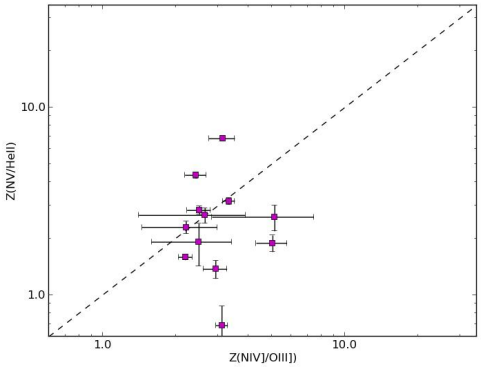

Fig. 48.— The comparison of the metallicities obtained from $\frac{NIV]}{OIII]}$ and $\frac{NV}{HeII}$. The dashed line is a representation of a 1-1 correlation.

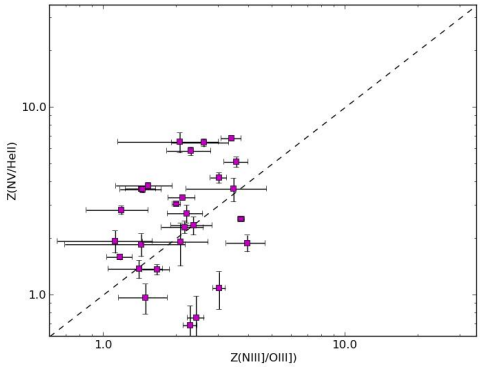

Fig. 49.— The comparison of the metallicities obtained from $\frac{NIII]}{OIII]}$ and $\frac{NV}{HeII}$. The dashed line is a representation of a 1-1 correlation.

D. $\frac{NV}{CIV}$ vs. $\frac{NV}{HeII}$ for the Segmented Power Law

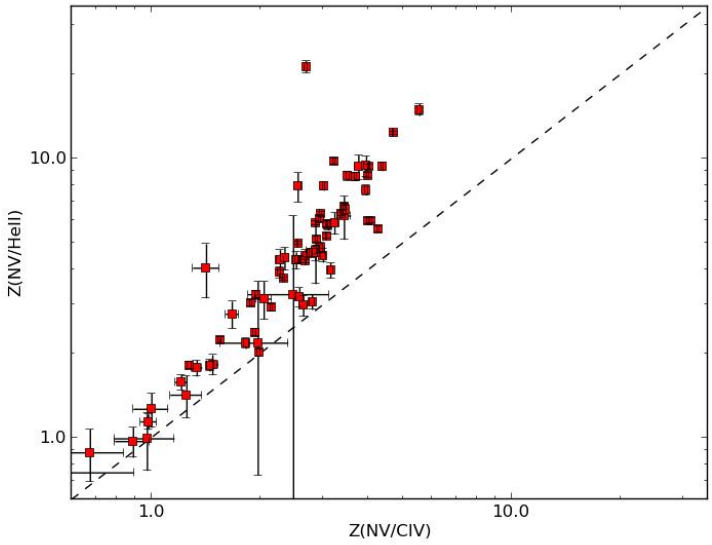

Fig. 50.— Comparison between the metallicity obtained from $\frac{NV}{CIV}$ and $\frac{NV}{HeII}$ respectively for the segmented continuum model.

E. Luminosity comparison of the continuum level at 1350 Å and 2100 Å

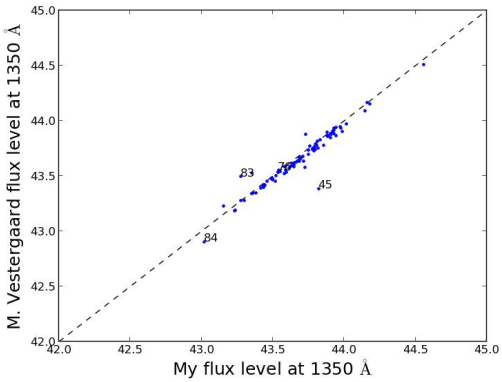

Fig. 51.— Comparison of the luminosity I obtained vs. the one obtained by M. Vestergaard for 1350 Å.

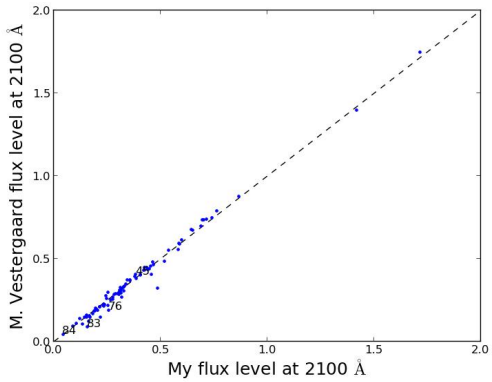

Fig. 52.— Comparison of the luminosity I obtained vs. the one obtained by M. Vestergaard for 2100 Å.

F. $\frac{FeII}{MgII}$-ratio to Redshift

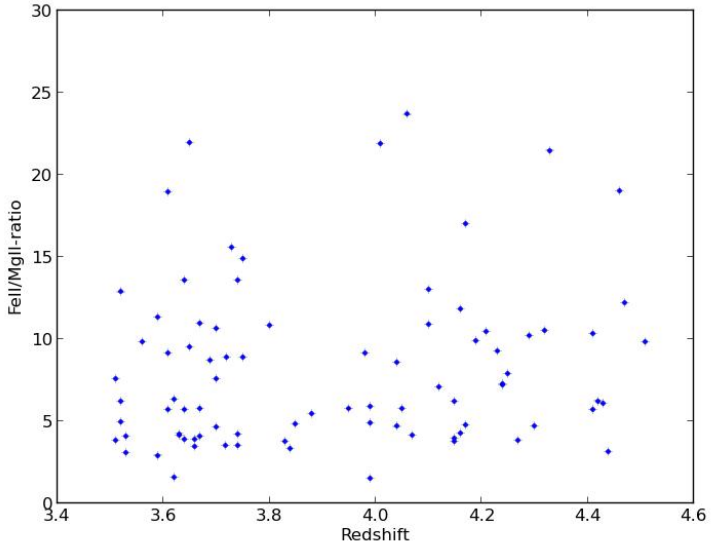

Fig. 53.— Comparison between the redshift and the $\frac{FeII}{MgII}$-ratio.

G. $\frac{FeII}{MgII}$-ratio to SMBH Mass

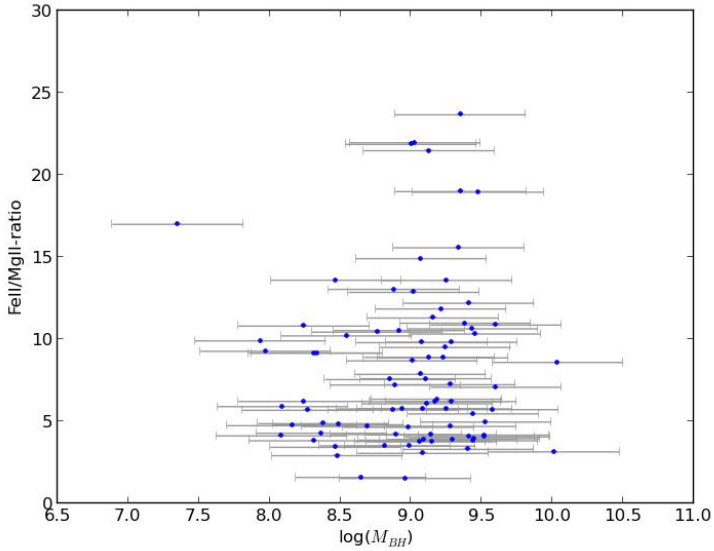

Fig. 54.— Comparison between the mass and the $\frac{FeII}{MgII}$-ratio.

H. $\frac{L_{bol}}{L_{edd}}$-Redshift

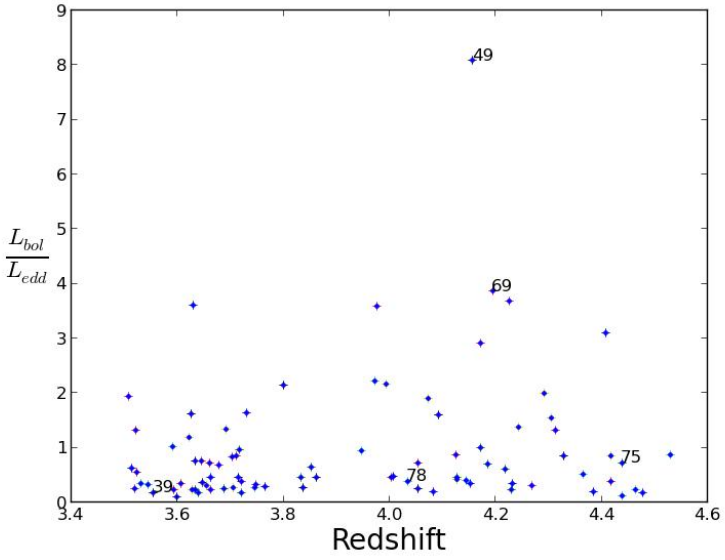

Fig. 55.— Comparison between the redshift and the $\frac{L_{bol}}{L_{edd}}$-ratio.